

Analysis of time integration methods for the compressible two-fluid model for pipe flow simulations



Benjamin Sanderse^{a,b,*}, Ivar Eskerud Smith^c, Maurice H.W. Hendrix^{a,d}

^a Shell Technology Centre Amsterdam, Amsterdam, The Netherlands

^b Centrum Wiskunde & Informatica (CWI), Amsterdam, The Netherlands

^c Norwegian University of Science and Technology (NTNU), Trondheim, Norway

^d Delft University of Technology, Delft, The Netherlands

ARTICLE INFO

Article history:

Received 9 March 2017

Revised 9 May 2017

Accepted 15 May 2017

Available online 25 May 2017

Keywords:

Two-fluid model

Time integration method

BDF2

Discrete flow pattern map

Stability

Von Neumann analysis

ABSTRACT

In this paper we analyse different time integration methods for the two-fluid model and propose the BDF2 method as the preferred choice to simulate transient compressible multiphase flow in pipelines. Compared to the prevailing Backward Euler method, the BDF2 scheme has a significantly better accuracy (second order) while retaining the important property of unconditional linear stability (A-stability). In addition, it is capable of damping unresolved frequencies such as acoustic waves present in the compressible model (L-stability), opposite to the commonly used Crank–Nicolson method. The stability properties of the two-fluid model and of several discretizations in space and time have been investigated by eigenvalue analysis of the continuous equations, of the semi-discrete equations, and of the fully discrete equations. A method for performing an automatic von Neumann stability analysis is proposed that obtains the growth rate of the discretization methods without requiring symbolic manipulations and that can be applied without detailed knowledge of the source code.

The strong performance of BDF2 is illustrated via several test cases related to the Kelvin–Helmholtz instability. A novel concept called Discrete Flow Pattern Map (DFPM) is introduced which describes the *effective* well-posed unstable flow regime as determined by the discretization method. Backward Euler introduces so much numerical diffusion that the theoretically well-posed unstable regime becomes numerically stable (at practical grid and timestep resolution). BDF2 accurately identifies the stability boundary, and reveals that in the nonlinear regime ill-posedness can occur when starting from well-posed unstable solutions. The well-posed unstable regime obtained in nonlinear simulations is therefore in practice much smaller than the theoretical one, which might severely limit the application of the two-fluid model for simulating the transition from stratified flow to slug flow. This should be taken very seriously into account when interpreting results from any slug-capturing simulations.

© 2017 Elsevier Ltd. All rights reserved.

1. Introduction

In the petroleum industry multiphase flow occurs when transporting oil and gas through long multiphase pipeline systems. The behaviour of the flow can take many forms, depending on parameters like fluid velocities, pipe properties and fluid properties. An important flow regime is (hydrodynamic) slug flow, in which liquid pockets, separated by gas bubbles, propagate in an alternating fashion with high speed along the pipeline. Such slugs have a large influence on the sizing of receiving facilities such as required

supports of the pipeline system and on the sizing of the downstream facilities such as separators (or slug catchers), compressors, pumps, and heat exchangers. The industry uses various flow models for simulating slug flow, but there is a need for increased accuracy. A promising approach is using so-called slug capturing, through the accurate numerical solution of the one-dimensional two-fluid model. Although this two-fluid model can become ill-posed, this approach is believed to be capable of describing the transition from stratified flow to slug flow, see e.g. Issa and Kempf (2003). The use of the compressible two-fluid model is necessary to generate slugs at the right frequency (Issa and Kempf, 2003).

Since the slug capturing approach is based on accurate solutions of the underlying model, higher order (higher than 1) numerical schemes or fine meshes are typically employed in both space and time. Different spatial discretization schemes have been

* Corresponding author at: Centrum Wiskunde & Informatica (CWI), Amsterdam, The Netherlands.

E-mail addresses: b.sanderse@cwi.nl (B. Sanderse), ivar.eskerud@gmail.com (I.E. Smith), m.h.w.hendrix@tudelft.nl (M.H.W. Hendrix).

used for the two-fluid model, for example the second-order central scheme (Liao et al., 2008), the QUICK scheme, a Roe scheme (Akselsen, 2016), a pseudo-spectral scheme (Holmås, 2010), and a Discontinuous Galerkin method (van Zwieten et al., 2015). The stability and accuracy properties of several of these schemes have been investigated recently by Fullmer et al. (2014); Liao et al. (2008); López de Bertodano et al. (2017) and Akselsen (2016). In all cases the incompressible model is discussed.

For the time integration of the two-fluid model, the workhorse in both industrial and academic codes has been the first order Backward Euler method, due to its stability and damping properties (Bendiksen et al., 1991; Danielson et al., 2005; Issa and Kempf, 2003; Montini, 2011). The large numerical diffusion, however, requires small time steps; the CFL number based on the liquid velocity is not on the order of 1 but has to be much smaller (Issa and Kempf, 2003; Liao et al., 2008). Only a few sources mention higher order time integration methods for the two-fluid model. Kjølås et al. (2013) mention that the slug-capturing module in LedaFlow (a commercial pipe flow simulator) uses the second order Crank–Nicolson method. Zou et al. (2015) employ the BDF2 (Backward Differentiation Formula) method for the two-fluid model to simulate the water faucet problem and found that it was superior to the first order Backward Euler method. However, a temporal accuracy study was only performed for a linear advection case, and for the other test cases the ‘basic’ two-fluid model (without level gradient terms) was used, which is unconditionally ill-posed. Also the commercial nuclear safety code RELAP-7 (Berry et al., 2015) advises BDF2 as the time integration method. However, almost no details are given on the stability, accuracy and damping properties of the numerical time integration method.

The purpose of this paper is to analyse different time integration methods for the compressible two-fluid model in terms of accuracy, stability and damping properties, and to use them to construct so-called discrete flow pattern maps. In particular, we show that BDF2 is preferred over Backward Euler and Crank–Nicolson because it combines second order accuracy with L -stability (filtering of acoustic waves at large time steps).

The paper is organized as follows: first, in Section 2 the two-fluid model is explained in terms of eigenvalues, stability and flow pattern maps. Section 3 describes the spatial (central, upwind) and temporal (Backward Euler, Crank–Nicolson, BDF2) discretizations used in this work. In Section 4 the stability and accuracy of the time integration methods are discussed by computing the eigenvalues of the spatial discretization and the stability domain of the time integration methods. Section 5 presents a von Neumann analysis applied to the fully discrete problem and a novel method to assess the stability without requiring symbolic manipulations. Section 6 presents three test cases: linear, nonlinear and acoustic wave growth based on Kelvin–Helmholtz instabilities. Section 7 provides concluding remarks.

2. Governing equations and characteristics

2.1. Compressible two-fluid model

The two-fluid model can be derived by considering mass and momentum balances for the stratified flow of oil and gas in a pipeline. The major assumption in the derivation is that of one-dimensional, stratified flow, with the transverse hydrostatic pressure variation introduced via level gradient terms. Furthermore, we assume isothermal flow so that no energy equation is required, and surface tension is neglected. In contrast to the incompressible model, which is commonly discussed in literature, we allow the gas phase to be compressible (the extension to compressible liquid is straightforward). This leads to the presence of acoustic waves in the solution, which in turn has an effect on the choice of time in-

tegration method, as will become clear later. With these assumptions, the two fluid model consists of the conservation equations for mass and momentum for the gas and liquid phase, reading:

$$\frac{\partial}{\partial t}(\rho_g A_g) + \frac{\partial}{\partial s}(\rho_g u_g A_g) = 0 \quad (1)$$

$$\frac{\partial}{\partial t}(\rho_l A_l) + \frac{\partial}{\partial s}(\rho_l u_l A_l) = 0 \quad (2)$$

$$\begin{aligned} \frac{\partial}{\partial t}(\rho_g u_g A_g) + \frac{\partial}{\partial s}(\rho_g u_g^2 A_g) \\ = -\frac{\partial p}{\partial s} A_g + LG_g - \tau_{gl} P_{gl} - \tau_g P_g - \rho_g A_g g_s + F_{body} A_g, \end{aligned} \quad (3)$$

$$\begin{aligned} \frac{\partial}{\partial t}(\rho_l u_l A_l) + \frac{\partial}{\partial s}(\rho_l u_l^2 A_l) \\ = -\frac{\partial p}{\partial s} A_l + LG_l + \tau_{gl} P_{gl} - \tau_l P_l - \rho_l A_l g_s + F_{body} A_l, \end{aligned} \quad (4)$$

supplemented with the volume equation:

$$A_g + A_l = A. \quad (5)$$

s is the spatial coordinate along the centerline of the pipe. The driving pressure force $F_{body} = -\frac{dp_{body}}{ds}$ in the gas and liquid momentum equations is required for the simulations that involve periodic boundary conditions. The friction models are described in Appendix A.2. The level gradient (LG) terms differ from the incompressible case and were derived and shown by us in van Zwieten et al. (2015); a similar form was presented in Masella et al. (1998):

$$LG_g = \frac{\partial HG_g}{\partial s}, \quad HG_g = \rho_g g_n \left[(R-h) A_g + \frac{1}{12} P_{gl}^3 \right], \quad (6)$$

$$LG_l = \frac{\partial HG_l}{\partial s}, \quad HG_l = \rho_l g_n \left[(R-h) A_l - \frac{1}{12} P_{gl}^3 \right]. \quad (7)$$

In Eqs. (1)–(7), the subscript β denotes the phase, either gas ($\beta = g$) or liquid ($\beta = l$). ρ_β denotes the density of phase β , A_β the cross-sectional area occupied by phase β , R the pipe radius, h the height of the liquid layer measured from the bottom of the pipe, u_β the phase velocity, p the pressure at the interface, τ_β the shear stress (with the wall or at the interface), g the gravitational constant, φ the local inclination of the pipeline with respect to the horizontal, $g_n = g \cos \varphi$ and $g_s = g \sin \varphi$. A_l (or A_g) and h are related by a non-linear algebraic expression since the pipeline has a circular cross-section (for channel flow one simply has $h = A_l$). Similarly, the wetted and interfacial perimeters P_g , P_l and P_{gl} can be expressed in terms of the hold-up or the interface height (see Appendix A.1 for more details). As a result, the two-fluid model features five equations with five unknowns (A_g , A_l , u_g , u_l , p). Depending on the velocity difference between the phases, the two-fluid model is well-posed or ill-posed (Barnea and Taitel, 1994; Lyczkowski et al., 1978; Stewart and Wendroff, 1984), as will be discussed in the next section.

2.2. Characteristics

The governing equations of the two-fluid model can be written in quasi-linear form in terms of the primitive variables $\mathbf{W} \in \mathbb{R}^q$ ($q = 4$),

$$\mathbf{W} = \begin{pmatrix} A_l \\ u_l \\ u_g \\ p \end{pmatrix}, \quad (8)$$

reading

$$\mathbf{A}(\mathbf{W}) \frac{\partial \mathbf{W}}{\partial t} + \mathbf{B}(\mathbf{W}) \frac{\partial \mathbf{W}}{\partial s} + \mathbf{C}(\mathbf{W}) = \mathbf{0}. \quad (9)$$

The eigenvalues can be found by substituting wave-like solutions in the homogeneous part of the equations (Drew and Passman, 1998; Hirsch, 1994), i.e. $\mathbf{W} = \hat{\mathbf{W}} e^{l(n_s s + n_t t)}$, leading to

$$\det(n_t \mathbf{A} + n_s \mathbf{B}) = 0. \quad (10)$$

By letting $\lambda = -n_t/n_s$ ($= \frac{ds}{dt}$) this can be seen as the generalized eigenvalue problem

$$\det(\mathbf{B} - \lambda \mathbf{A}) = 0. \quad (11)$$

Compact expressions for the eigenvalues are difficult to obtain analytically since the characteristic equation is quartic. Evje and Flåtten (2003) derived approximate expressions using a perturbation technique suggested by Toumi and Kumbaro (1996), but did not include the level gradient terms (while their inclusion is essential for well-posedness). When considering an incompressible liquid and a compressible gas, while neglecting the hydraulic gradient term in the gas phase and using the ‘incompressible’ form of the hydraulic gradient of the liquid phase, a simple expression for the characteristic equation can be obtained (see also Figueiredo et al., 2017):

$$A_g(c_g^2 - (\lambda - u_g)^2) \left(\frac{\partial H G_l}{\partial A_l} + \rho_l(\lambda - u_l)^2 \right) + A_l c_g^2 \rho_g (\lambda - u_g)^2 = 0. \quad (12)$$

Here c_g is the speed of sound of the gas phase ($\rho_g = p/c_g^2$). In our simulations we continuously check the well-posedness of the model by computing the eigenvalues from a quartic which is similar to (12), but which includes all compressibility and hydraulic gradient effects. When complex eigenvalues are encountered, the simulation is stopped, since we take the view of Drew and Passman (1998) that the original initial boundary value problem has become meaningless. The four eigenvalues are typically ordered as follows:

$$\lambda_1 \leq \lambda_2 \leq \lambda_3 \leq \lambda_4, \quad (13)$$

where λ_1 and λ_4 are related to the speed of sound of the gas, and λ_2 and λ_3 are related to the convective wave speeds. The problem contains therefore two distinctly different time scales:

$$|\lambda_1|, |\lambda_4| \gg |\lambda_2|, |\lambda_3|, \quad (14)$$

with a typical ratio of $\mathcal{O}(10^2) - \mathcal{O}(10^3)$. For slightly compressible flow, the eigenvalues λ_2 and λ_3 are expected to be close to the incompressible expressions, see for example (Bonizzi, 2003). These incompressible roots are given by

$$\lambda_{2,3} = \frac{(\rho u)^* \pm \xi}{\rho^*}, \quad (15)$$

where, in the notation from Akselsen (2016):

$$\xi^* = \frac{\zeta_l}{A_l} + \frac{\zeta_g}{A_g}, \quad (16)$$

and

$$\xi = \sqrt{\rho^*(\rho_l - \rho_g)g_n \frac{\partial h}{\partial \alpha_l} - \frac{\rho_g \rho_l}{A_g A_l} (u_g - u_l)^2}. \quad (17)$$

The incompressible two-fluid model is therefore well-posed as long as the velocity difference between the phases is smaller than the ‘inviscid Kelvin–Helmholtz’ limit (IKH) (Liao et al., 2008):

$$(u_g - u_l)^2 \leq \Delta U_{\text{IKH}}^2 = \frac{(\rho_l - \rho_g)}{\rho^*} g_n \frac{\partial h}{\partial \alpha_l}. \quad (18)$$

The compressibility of the gas hardly changes this limit (Bonizzi, 2003). The compressible two-fluid model under consideration is therefore conditionally well-posed. Several remedies have been proposed to make it unconditionally well-posed:

- An artificial interfacial pressure term (Evje and Flåtten, 2003); this is a mathematical ‘trick’ which eliminates the growth of interfacial waves due to Kelvin–Helmholtz instabilities (Fullmer et al., 2014; Liao et al., 2008).
- Surface tension (Ramshaw and Trapp, 1978); next to well-posed the model is also stable for small scale perturbations below a cut-off wavelength. However, between this cut-off wavelength and the IKH wavelength the model is unstable (Fullmer et al., 2014) and when sufficiently fine grids are used in numerical simulations, these short-wavelength instabilities are resolved and will grow (Holmås, 2008).
- Diffusive terms, either artificial (Holmås, 2008) or physical (Fullmer et al., 2014). Although this has certain advantages, such as nonlinear stability, the growth rate for short waves is very large, making the model practically ill-posed (Fullmer et al., 2014).

Other approaches are the use of a virtual mass force (Montini, 2011), a momentum flux parameter (Song, 2003; Song and Ishii, 2001) and a two-pressure model (Fitt, 1989; Ransom and Hicks, 1984; 1988). The ‘best’ remedy is still the subject of debate in the two-fluid model community. In this paper the focus is on the accurate time-integration of the conditionally well-posed model (1)–(4) and we do not make attempts to make the model unconditionally well-posed.

2.3. Stability

To investigate the stability of the equations of the two-fluid model we take the following approach (Montini, 2011; Ramshaw and Trapp, 1978): linearization of the governing equations around a reference state, assuming a travelling wave solution for the perturbations, and determining the dispersion relation to identify the stability. A similar approach is taken in Liao et al. (2008) and Fullmer et al. (2014).

We linearize the governing equations by writing $\mathbf{W} = \mathbf{W}_0 + \tilde{\mathbf{W}}$ (where $\tilde{\mathbf{W}} \ll \mathbf{W}_0$), using the fact that the reference state (indicated by $(\cdot)_0$) satisfies the equations, and neglecting products of disturbances. The linearized equations then read:

$$\mathbf{A}_0 \frac{\partial \tilde{\mathbf{W}}}{\partial t} + \mathbf{B}_0 \frac{\partial \tilde{\mathbf{W}}}{\partial s} = \mathbf{C}_0 \tilde{\mathbf{W}}, \quad (19)$$

where $\mathbf{A}_0 = \mathbf{A}(\mathbf{W}_0)$, $\mathbf{B}_0 = \mathbf{B}(\mathbf{W}_0)$, and $\mathbf{C}_0 = \left(\frac{\partial \mathbf{C}}{\partial \mathbf{W}} \right)_0$. It is cumbersome to determine \mathbf{C}_0 analytically due to the presence of the friction factors, see Eq. (A.7), and in general we determine it numerically.

The perturbation is assumed to be of a wave like form: $\tilde{\mathbf{W}} = \mathbf{e} e^{l(\omega t - ks)}$, with ω being the angular frequency and k the wave number. This leads to

$$(\mathbf{A}_0 \cdot (l\omega) - \mathbf{B}_0 \cdot (lk) - \mathbf{C}_0) \mathbf{e} e^{l(\omega t - ks)} = 0. \quad (20)$$

For non-trivial solutions we need

$$\det(\mathbf{A}_0 \cdot (l\omega) - \mathbf{B}_0 \cdot (lk) - \mathbf{C}_0) = 0. \quad (21)$$

This yields the dispersion relation $\omega(k)$. In the absence of source terms ($\mathbf{C}_0 = 0$), the condition for stability ($\text{Im}(\omega) = 0$) is equivalent to the IKH well-posedness limit (18) obtained from the eigenvalue analysis. The dispersion analysis presented here is based on the full set of conservation equations and the resulting KH instability is therefore a so-called dynamic instability (Lopez-de-Bertodano et al., 2013). When source terms are included, the stability condition differs from the well-posedness criterion and the stability

Table 1

Parameter values used in the example of the Kelvin–Helmholtz problem.

Parameter	Value	Unit
α_l	0.5	[-]
u_g	13.815	m/s
u_l	1	m/s
ρ_l	1000	kg/m ³
R	0.039	m
p_0	10 ⁵	N/m ²
c_g	293.43	m/s
g	9.8	m/s ²
μ_g	$1.8 \cdot 10^{-5}$	Pa s
μ_l	$8.9 \cdot 10^{-4}$	Pa s
ϵ	10^{-8}	m
F_{body}	74.225	Pa/m

limit is commonly known as the viscous Kelvin–Helmholtz (VKH) stability limit. This ‘viscous’ instability is similar to the kinematic waves in shallow water theory (Whitham, 1974) and the continuity waves of Wallis (1969).

2.4. Flow pattern map

An example of the IKH and VKH stability boundaries will be given here for the compressible equations in terms of a flow pattern map. We consider the Kelvin–Helmholtz instability problem, at the same conditions as proposed and analyzed by Liao et al. (2008). A horizontal pipe with a length of one meter is taken ($\varphi = 0$) and its diameter is 78 mm. The density of the gas is given by a perfect gas relation,

$$\rho_g = \frac{p}{c_g^2}, \quad (22)$$

where c_g is taken such that for $p = p_0$ we have $\rho_g = 1.1614 \text{ kg/m}^3$. The density of the liquid is constant (incompressible). The superficial liquid velocity is set at 0.5 m/s, and the superficial gas velocity at $u_{sg} = 6.908 \text{ m/s}$. The liquid hold-up, gas velocity, liquid velocity and pressure gradient follow from the steady state momentum balance and are given, together with other parameters, in Table 1. Note that ϵ is the hydraulic wall roughness, and μ is the fluid viscosity.

Liao et al. (2008) report that the stability limit (18) for the incompressible model is $\Delta U_{\text{IKH}} = 16.0768 \text{ m/s}$. In the compressible model the stability limit slightly changes to $\Delta U_{\text{IKH}} = 16.0355 \text{ m/s}$. Since at the current conditions $\Delta U = 12.815 \text{ m/s}$, the model is well-posed and stable. Note that we have employed Biberg’s approximate relation for $\alpha_l(h)$, see Eq. (A.5), which leads to a small difference in the stability limit compared to the nonlinear relation.

We consider a single wave with $k = 2\pi$ on a domain $s \in [0, 1] \text{ m}$. The dispersion analysis, Eq. (20), then leads to 4 waves with the following eigenvalues and angular frequencies:

$$\lambda = \begin{pmatrix} -279.80 \\ 0.69 \\ 1.34 \\ 307.40 \end{pmatrix} \text{ m/s}, \quad \omega = \begin{pmatrix} -1758.05 \\ 4.27 \\ 8.48 \\ 1931.47 \end{pmatrix} + \begin{pmatrix} 4.51i \\ 0.59i \\ -0.35i \\ 4.71i \end{pmatrix} 1/\text{s}. \quad (23)$$

The fact that all eigenvalues are real indicates that the initial condition is indeed well-posed, with $\lambda_{1,4}$ close to the speed of sound of the gas and $\lambda_{2,3}$ close to the liquid velocity. The angular frequencies indicate that out of the four waves there is one unstable mode, ω_3 , which will grow in time.

When repeating this analysis for different superficial liquid and gas velocities the neutral IKH and VKH stability boundaries can be constructed according to $\text{Im}(\omega) = 0$ – see Fig. 1. These neutral stability boundaries are independent of the wave number k

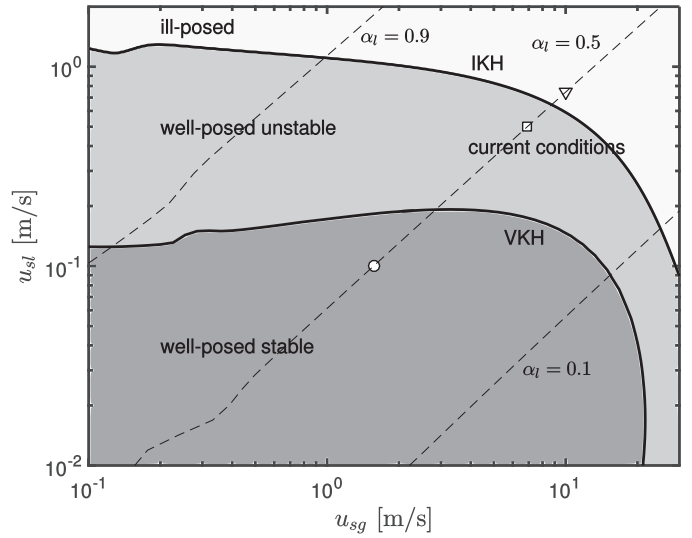


Fig. 1. Flow pattern map based on Kelvin–Helmholtz instabilities. The symbols ○, □ and ▽ correspond to the lines in Fig. 2.

(Barnea and Taitel, 1994; Prosperetti and Tryggvason, 2007). In between the inviscid and viscous stability curves we have a well-posed, unstable solution of the two-fluid model, in which transition from stratified flow to slug flow can possibly occur. The conditions given in Table 1 are indicated by ‘current conditions’ and they are in this well-posed, unstable regime. Lines of constant hold-up are indicated by dashes in Fig. 1. The resulting flow pattern map and lines are similar to those of Barnea and Taitel (1993). In Fig. 2 the dispersion relation associated to the current conditions is shown (square symbol), together with the dispersion relation for a point in the well-posed stable regime (round symbol) and a point in the ill-posed regime (triangle). On the left (Fig. 2a) ω is plotted as a function of wavelength λ , in a similar way as in Fullmer et al. (2014). This confirms that for short waves ($\lambda \rightarrow 0$) the ill-posed model possesses unbounded growth, whereas the well-posed unstable model has a bounded growth rate ($\text{Im}(\omega_3) = -0.35/\text{s}$). In all cases the most unstable ω is shown, which corresponds to ω_3 (for the stable case this is the least stable mode). On the right (Fig. 2b) the same plot is shown, but now as a function of k , similar to Liao et al. (2008). This latter form of the dispersion relation will be used in our numerical results.

3. Spatial and temporal discretization

3.1. Finite volume method on a staggered grid

As mentioned in the introduction, many options are available for the spatial discretization of the two-fluid model, such as finite difference methods (Fullmer et al., 2014; Liao et al., 2008), pseudo-spectral methods (Holmås, 2010), and characteristics methods (Akselsen, 2016). We discretize the two-fluid model, Eqs. (1)–(4), by using a finite volume method on a staggered grid. As indicated in Fig. 3, the staggered grid consists of both p -volumes, Ω^p , and u -volumes, Ω^u . Each volume consists of a liquid and a gas phase: $\Omega = \Omega_l \cup \Omega_g$, for both u - and p -volumes.

We start with conservation of mass for a phase β (β is liquid or gas). Integration of Eq. (1) in s -direction over a p -volume gives:

$$\frac{d}{dt} (\rho_{\beta,i} \Omega_{\beta,i}) + (\rho_{\beta} A_{\beta})_{i+1/2} u_{\beta,i+1/2} - (\rho_{\beta} A_{\beta})_{\beta,i-1/2} u_{\beta,i-1/2} = 0, \quad (24)$$

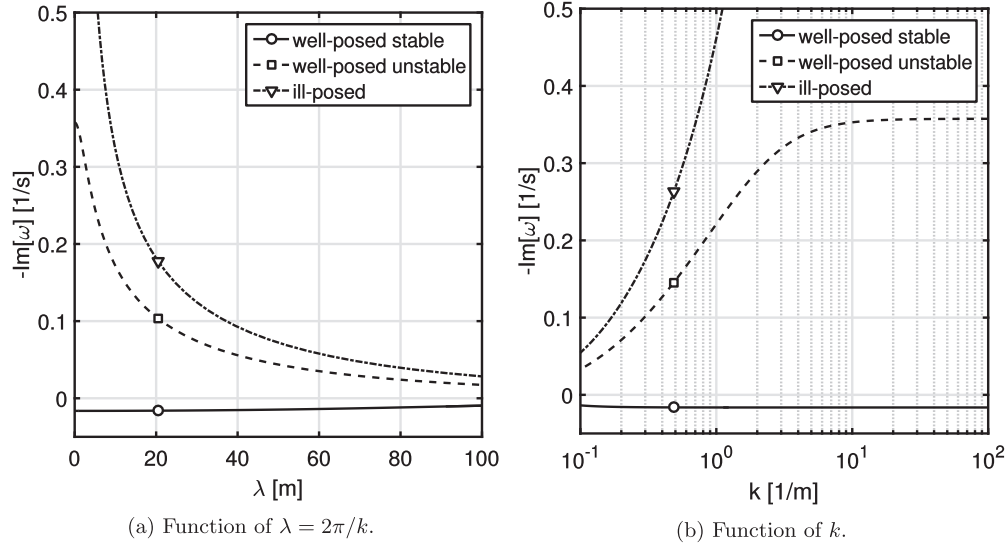


Fig. 2. Dispersion relation for well-posed stable, well-posed unstable, and ill-posed model, corresponding to the points shown in Fig. 1.

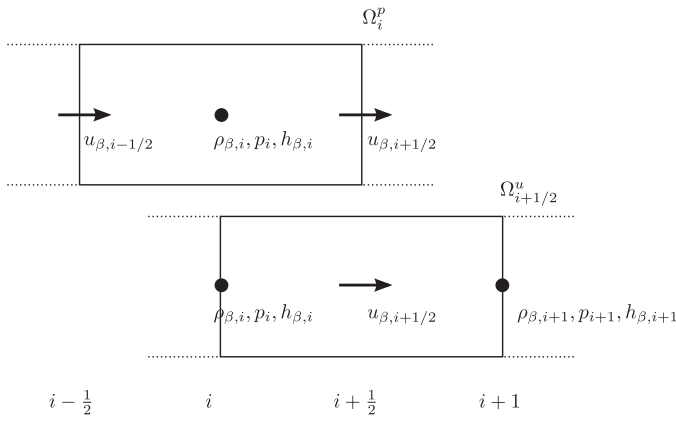


Fig. 3. Staggered grid layout.

with the finite volume size given by

$$\Omega_{\beta,i} = A_{\beta,i} \Delta s_i. \quad (25)$$

The term $(\rho_{\beta} A_{\beta})_{i+1/2}$ requires interpolation from neighbouring values, which is described below. For conservation of momentum we proceed in a similar way. Integration of (3) in s -direction over a u -volume gives:

$$\begin{aligned} \frac{d}{dt} (\rho_{\beta,i+1/2} u_{\beta,i+1/2} \Omega_{\beta,i+1/2}) + (\rho_{\beta} A_{\beta})_{i+1} (u_{\beta,i+1})^2 \\ - (\rho_{\beta} A_{\beta})_i (u_{\beta,i})^2 = -A_{\beta,i+1/2} (p_{i+1} - p_i) + LG_{\beta,i+1/2} \\ - \rho_{\beta,i+1/2} \Omega_{\beta,i+1/2} g_s - \sum_{\gamma \in \{L,G,W\}} \tau_{\beta\gamma,i+1/2} p_{\beta\gamma,i+1/2} \Delta s_{i+1/2} \\ + A_{\beta,i+1/2} F_{\text{body}} \Delta s_{i+1/2}, \end{aligned} \quad (26)$$

where

$$\Omega_{\beta,i+1/2} = A_{\beta,i+1/2} \Delta s_{i+1/2}. \quad (27)$$

and the level gradient terms for the gas and liquid are given by (+ for gas, – for liquid)

$$LG_{\beta,i+1/2} = g \cos(\varphi) \left(\left(h A_{\beta} \pm \frac{1}{12} p_{gl}^3 \right)_i - \left(h A_{\beta} \pm \frac{1}{12} p_{gl}^3 \right)_{i-1} \right), \quad (28)$$

Several terms in (24) and (26) require approximation. All terms that are not part of the convective terms are interpolated using a central scheme, e.g. $A_{\beta,i+1/2} = \frac{1}{2} (A_{\beta,i} + A_{\beta,i+1})$. The convective terms, on the other hand, require more care in order to

prevent numerical oscillations. Since the system under consideration is (conditionally) hyperbolic, the wave directions have to be taken into account in the differencing scheme, e.g. by using a Roe method (Akselsen, 2016; Morin et al., 2013). In this work the focus is on the time integration method and we employ standard spatial discretization methods for the convective quantities: first order upwind or second order central. The central scheme is accurate and stable in our computations since the solutions to the test cases are sufficiently smooth, i.e. we are not simulating discontinuities or flow transitions.

The spatial discretization presented in this section leads to a semi-discrete system, only depending on time, which can be written as

$$\frac{d\mathbf{U}}{dt} = \mathbf{F}(\mathbf{U}), \quad (29)$$

where $\mathbf{U} = \mathbf{U}(t) \in \mathbb{R}^{qN}$ is the vector of conserved variables. For periodic boundary conditions, which we will consider, it reads

$$\mathbf{U} = [(\rho_g A_g \Delta s)_{1,\dots,N}, (\rho_l A_l \Delta s)_{1,\dots,N}, (\rho_g A_g u_g \Delta s)_{1/2,\dots,N-1/2}, (\rho_l A_l u_l \Delta s)_{1/2,\dots,N-1/2}]^T. \quad (30)$$

We use \mathbf{U} instead of \mathbf{W} in a discrete setting to ensure discrete conservation properties.

3.2. Temporal discretization

Eq. (29) forms a system of ordinary differential equations which can be integrated in time with many different time integration methods (Butcher, 2003; Hairer et al., 2008). A common distinction is between multi-stage methods (Runge–Kutta) and multi-step methods (Adams, Backward Differentiation Formula (BDF)). Within both classes there is a distinction between explicit and implicit methods. Due to the strong time step restriction for explicit methods (caused by the acoustic speeds λ_1 and λ_4), we consider implicit methods. For the two-fluid model, the Backward Euler method is widely applied because of its unconditional numerical stability characteristics, although it has the disadvantage of being only first-order accurate, which introduces a significant amount of numerical diffusion. To construct a second order method that keeps the good stability properties, one can see Backward Euler as a member of the family of implicit Runge–Kutta methods, as a member of the Adams–Moulton methods, or as member of the BDF methods. A second order extension of Backward Euler can be

Table 2
Parameter values for time integration methods.

scheme	a_0	a_1	a_2	θ
Backward Euler	1	−1	0	1
BDF2	$\frac{3}{2}$	−2	$\frac{1}{2}$	1
Crank–Nicolson	1	−1	0	$\frac{1}{2}$

sought in each of these families. We restrict ourselves to Crank–Nicolson and BDF2, which are both second order accurate and unconditionally stable. Backward Euler, Crank–Nicolson and BDF2 can all be gathered under the following expression:

$$\frac{a_0 \mathbf{U}^{n+1} + a_1 \mathbf{U}^n + a_2 \mathbf{U}^{n-1}}{\Delta t} = \theta \mathbf{F}(\mathbf{U}^{n+1}, t^{n+1}) + (1 - \theta) \mathbf{F}(\mathbf{U}^n, t^n). \quad (31)$$

with the parameter values given in Table 2. The local truncation error for the methods is given by

$$\tau_{\text{BE,CN}} = \left(\theta - \frac{1}{2}\right) \Delta t^2 \mathbf{F}'' + \left(\frac{1}{2}\theta - \frac{1}{3}\right) \Delta t^3 \mathbf{F}''' + \mathcal{O}(\Delta t^4), \quad (32)$$

$$\tau_{\text{BDF2}} = -\frac{2}{9} \Delta t^3 \mathbf{F}''' + \mathcal{O}(\Delta t^4). \quad (33)$$

The leading error constant of Crank–Nicolson is $\frac{1}{12}$, which is smaller than that of BDF2.

Eq. (31) is a system of nonlinear equations and application of Newton's method leads to the following linear system that is solved at each time step:

$$\left[\frac{a_0}{\Delta t} \mathbf{I} - \theta \left(\frac{\partial \mathbf{F}}{\partial \mathbf{U}} \right)^m \right] \Delta \mathbf{U} = - \left[\frac{a_0 \mathbf{U}^m + a_1 \mathbf{U}^n + a_2 \mathbf{U}^{n-1}}{\Delta t} - \theta \mathbf{F}(\mathbf{U}^m, t^{n+1}) - (1 - \theta) \mathbf{F}(\mathbf{U}^n, t^n) \right], \quad (34)$$

where m is the iteration counter. If the direct evaluation of \mathbf{F} in terms of \mathbf{U} is not possible - for example in the case of a nonlinear equation of state, when the pressure cannot easily be obtained from the density - we solve Eq. (34) in terms of \mathbf{W} , which requires the evaluation of an additional Jacobian. Solving system (34) has roughly the same computational cost for Backward Euler, Crank–Nicolson and BDF2. This is because the evaluation of the Jacobian is the most expensive part, which is the same for all methods since they are all implicit in time. From an implementation point of view, BDF2 can be implemented relatively easily in an existing code that uses Backward Euler, because the only extra required variable is \mathbf{U}^{n-1} .

The BDF2 method suffers from a start-up problem: \mathbf{U}^{n-1} is not available at the first time step, which is therefore computed with Backward Euler. Note that for variable time steps the coefficients of the BDF2 method become dependent on the time step ratio. Another issue of BDF2 is the fact that it is not unconditionally monotone (neither is Crank–Nicolson), and therefore under- or overshoots can appear near discontinuities (Hundsdoerfer and Verwer, 2007; Zou et al., 2015). Adaptive time stepping or locally using Backward Euler are possible solutions to this issue. In the test cases reported here this was not required.

3.3. Reference solution with explicit Runge–Kutta method

A highly accurate reference solution in time is obtained by employing an explicit Runge–Kutta method. Explicit methods are normally not of interest for the compressible equations due to the time step restriction associated with the acoustic waves, but in the case that these waves are to be resolved (as we will do in one

Table 3
Case definition for analysis of stiffness of semi-discrete equations.

Case	N	u_{sl}, u_{sg} [m/s]	c_g [m/s]	Convective terms
I	40	0.5, 6.908	$c_{g,0}$	Central
Ila	20	0.5, 6.908	$c_{g,0}$	Central
Ilb	80	0.5, 6.908	$c_{g,0}$	Central
IIla	40	0.5, 6.908	$0.1 c_{g,0}$	Central
IIlb	40	0.5, 6.908	$10 c_{g,0}$	Central
IV	40	0.5, 6.908	$c_{g,0}$	Upwind
V	40	0.05, 0.829	$c_{g,0}$	Central

of the test cases), they provide a cheap and highly accurate alternative to implicit methods. A general s -stage explicit Runge–Kutta method applied to (29) reads:

$$\mathbf{U}^{n+1} = \mathbf{U}^n + \Delta t \sum_{i=1}^s b_i \mathbf{F}(\mathbf{U}_i, t_i), \quad (35)$$

where

$$\mathbf{U}_i = \mathbf{U}^n + \Delta t \sum_{j=1}^s a_{ij} \mathbf{F}(\mathbf{U}_j, t_j), \quad t_i = t^n + c_i \Delta t. \quad (36)$$

We have used a three-stage, third order strong-stability preserving Runge–Kutta method (Gottlieb et al., 2001) with the following non-zero coefficients: $a_{21} = 1$, $a_{31} = a_{32} = \frac{1}{4}$, $b_1 = b_2 = \frac{1}{6}$, $b_3 = \frac{2}{3}$.

4. Time scales, stability and stiffness

4.1. Spectrum of the spatial discretization

The distinct time scales of the problem, see Eq. (14), make the semi-discrete Eqs. (29) stiff: some terms in the differential equations lead to very fast transients, while others are much slower. In order to investigate the stiffness induced by the problem and the spatial discretization (without including the effect of the temporal discretization yet) we look at the eigenvalues of the semi-discrete equations. Similar to the stability analysis of Section 2.3, we linearize the semi-discrete equations around a background state (for example the initial condition): $\mathbf{U}(t) = \mathbf{U}_0 + \tilde{\mathbf{U}}(t)$, which gives

$$\frac{d\tilde{\mathbf{U}}}{dt} = \mathbf{J}\tilde{\mathbf{U}}, \quad (37)$$

with $\mathbf{J} = \left(\frac{\partial \mathbf{F}}{\partial \mathbf{U}} \right)_0 \in \mathbb{R}^{qN \times qN}$. Diagonalization of $\mathbf{J} = \mathbf{K}\mathbf{D}\mathbf{K}^{-1}$ leads to the following set of decoupled equations:

$$\frac{d\tilde{\mathbf{Z}}}{dt} = \mathbf{D}\tilde{\mathbf{Z}}, \quad (38)$$

where $\mathbf{Z} = \mathbf{K}^{-1}\mathbf{U}$. The matrix \mathbf{D} is a diagonal matrix with the eigenvalues μ of \mathbf{J} . These eigenvalues μ are the discrete approximation of the eigenvalues of only the spatial derivatives of the two-fluid model equations, based on Fourier analysis. For example, a convective term of the form $c \frac{\partial}{\partial s}$ leads to purely imaginary eigenvalues of the form $-cl$. Diffusive phenomena on the other hand are associated to negative real eigenvalues, and unstable solutions to $\text{Re}(\mu) > 0$. Therefore, in contrast to the eigenvalues λ of the continuous equations, complex eigenvalues μ of the semi-discrete equations are not associated to well- or ill-posedness.

We investigate the behaviour of the eigenvalues μ of the spatial discretization by performing parametric studies on the well-posed, unstable Kelvin–Helmholtz problem for which the conditions where given in Table 1. The considered cases are specified in Table 3. Case I in Table 3 with $N = 40$ finite volumes and a central discretization of the convective terms is considered as the base case. Four additional cases are defined, in which the effect of the grid size, gas compressibility, upwind scheme and VKH stability on

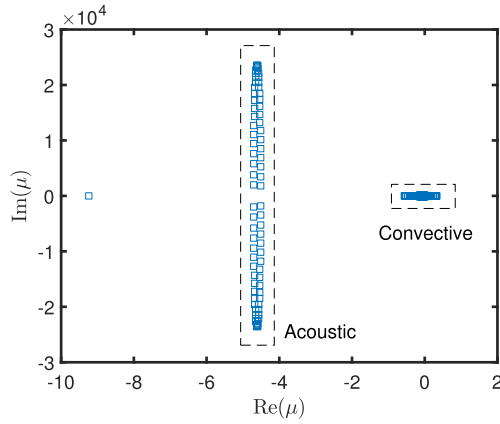


Fig. 4. Eigenvalues for case I.

the eigenvalues is investigated. The eigenvalues $\mu(\mathbf{J})$ are computed numerically with Matlab for all cases.

The $4N$ ($=160$) eigenvalues for case I are shown in Fig. 4, with zoomed-in details for the $\approx 2N$ acoustic modes and $\approx 2N$ convective modes in Figs. 5a and 5b, respectively. Some convective modes have a positive real part, indicating that certain solution components will grow in time. The central discretization thus captures the fact that the initial condition is in the well-posed unstable regime. The real part of the acoustic eigenvalues corresponds to the imaginary part of the angular frequencies ω_1 and ω_4 (see Eq. (23)). Similarly, the real part of the convective eigenvalues corresponds to the imaginary part of ω_2 and ω_3 . The imaginary parts of the acoustic and convective eigenvalues differ by several orders of magnitude. This corresponds to the fact that the acoustic modes have a much higher frequency than the convective modes. The semi-discrete equation system is therefore stiff and requires a suitable time integration method, as will be detailed in Section 4.

The stiffness of the problem depends on the grid size. This is shown in Fig. 5, which compares the eigenvalues for 20 grid points (6a) and for 80 grid points (6b). The finer the grid, the larger the imaginary part of the eigenvalues, and the higher the frequencies that can be represented numerically. The scaling of the imaginary part of the eigenvalues is linear in the number of grid points, and when an explicit time integration method is used this leads to a CFL-type stability condition: $\Delta t = \mathcal{O}(\Delta s)$. The fact that the real part of the eigenvalues is not affected by the grid size confirms that there is no numerical diffusion added when the central scheme for the convective terms is employed.

Next to the grid size, the gas compressibility has a large effect on the stiffness of the problem. Figs. 7 show the results for a more compressible (Fig. 7b) and a less compressible (Fig. 7c) case. The larger the degree of incompressibility, the higher the ratio between the imaginary part of the eigenvalues of the acoustic and convective modes. The effect of making the gas more incompressible is similar to refining the grid: the scaling of the imaginary part of the eigenvalues is linear in the speed of sound of the gas.

It is now interesting to see how the eigenvalues change when the first-order upwind spatial discretization, instead of the central discretization, is considered. Fig. 8 shows that the real part of the eigenvalues of both the acoustic and convective modes has grown enormously, indicating the numerical damping caused by the upwind scheme. The damping of the first order upwind method is in fact so large that almost all unstable modes have shifted to the left half of the complex plane. These observations are in line with Liao et al. (2008), who favour the central discretization for the accurate prediction of the stability of the two-fluid model.

Lastly, we consider the case where the superficial velocities are reduced so that the initial condition is in the well-posed stable regime. Fig. 9 shows that, employing once again the central scheme, all eigenvalues have a negative real part. This indicates a stable solution, in agreement with its position in the flow pattern map. The eigenvalues are organized in two ellipses, which is typical for travelling waves that are damped in time. Note that all the eigenvalues fall on the imaginary axis when the source terms are switched off (giving the inviscid two-fluid model) and the central scheme is used; this means that the solution consists of pure travelling waves. Thus, the friction terms in the equations are responsible for the damping of both the acoustic and the convective waves.

4.2. Stability properties of the time integration methods

For a stable time integration of the semi-discrete two-fluid model, the eigenvalues of the spatial discretization shown in Figs. 4–9 should fall inside the stability region of the time integration method. This stability region follows by application of the time integration method described by Eq. (31) to a linear test equation (as derived from Eq. (38)):

$$\dot{v}(t) = \mu v(t), \quad \mu \in \mathbb{C}, \quad (39)$$

and computing the amplification factor:

$$G(z) = \left| \frac{v^{n+1}}{v^n} \right|, \quad z = \mu \Delta t. \quad (40)$$

This amplification factor indicates whether the numerical solution will grow in time. The exact solution to Eq. (39) is stable when $\text{Re}(\mu) < 0$. A time integration scheme that inherits this property is called unconditionally stable or *A*-stable when stable solutions to the ODE (39) are obtained in a stable manner by the time integration method, for all choices of Δt . This can be expressed as:

$$\text{\$A\$-stable: } G(z) \leq 1 \quad \text{for } \text{Re}(z) \leq 0. \quad (41)$$

Next to *A*-stability, the concept of *L*-stability is important since we are dealing with a stiff system. *L*-stability indicates whether unresolved (very high) frequencies are damped by the numerical method. In terms of the amplification factor *G* it reads

$$\text{\$L\$-stable: } G(z) \rightarrow 0 \quad \text{when } \text{Re}(z) \rightarrow -\infty. \quad (42)$$

Application of the time integration method expressed by Eq. (31) to the test Eq. (39) leads to the following equation for *G*:

$$(a_0 - \mu \Delta t \theta) G^2 + (a_1 - \mu \Delta t (1 - \theta)) G + a_2 = 0. \quad (43)$$

The amplification factor can be displayed as a contour in the complex $z = \mu \Delta t$ space (see any standard textbook on time integration methods, e.g. Butcher (2003); Hairer et al. (2008)). Here we take a slightly different approach: we set a certain time step and display *G* in complex μ space instead of $\mu \Delta t$ space. This allows direct comparison with the eigenvalues of the semi-discrete equations (see case I in Fig. 4). For the specific case that the time step is based on the liquid velocity ($\Delta t = 1/40$ s), and not on the speed of sound, Figs. 10a–10c show the eigenvalue locations and the corresponding amplification factor. The vertical axis is on log-scale and only the positive imaginary part is shown (all eigenvalues appear as complex conjugates). Fig. 10 shows that all the three considered methods are *A*-stable, since $G < 1$ in the left half part of the complex plane. Crank–Nicolson is the only method which will give, independent of Δt , the correct unstable solutions to (39) for all z when $\text{Re}(z) > 0$. For BDF2 and Backward Euler the time step has to be sufficiently small so that the eigenvalues move into the region $G > 1$. Since the two-fluid model with friction terms can exhibit unstable solutions (Fig. 5b), with eigenvalues in the right-half of the complex plane, this is a desirable feature.

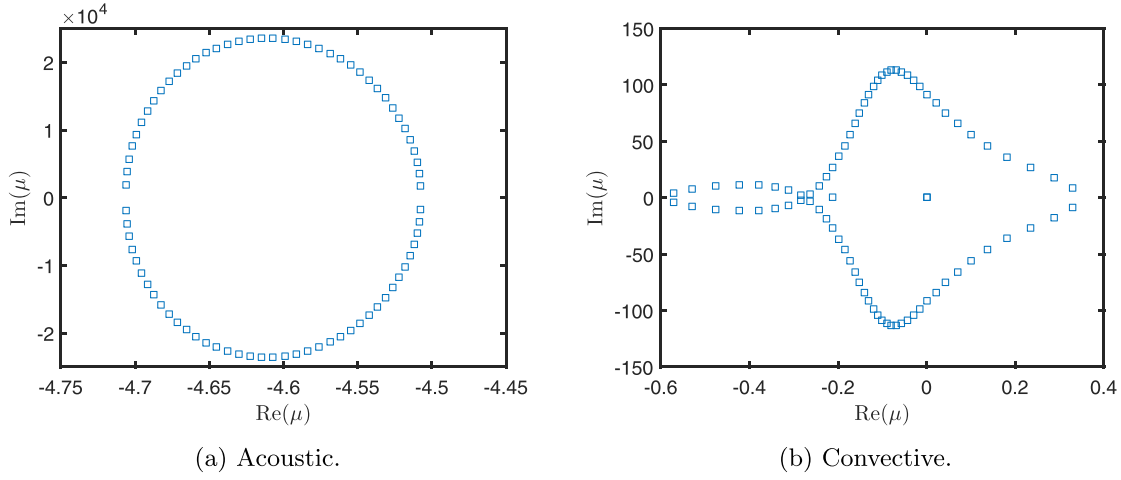


Fig. 5. Details of Fig. 4.

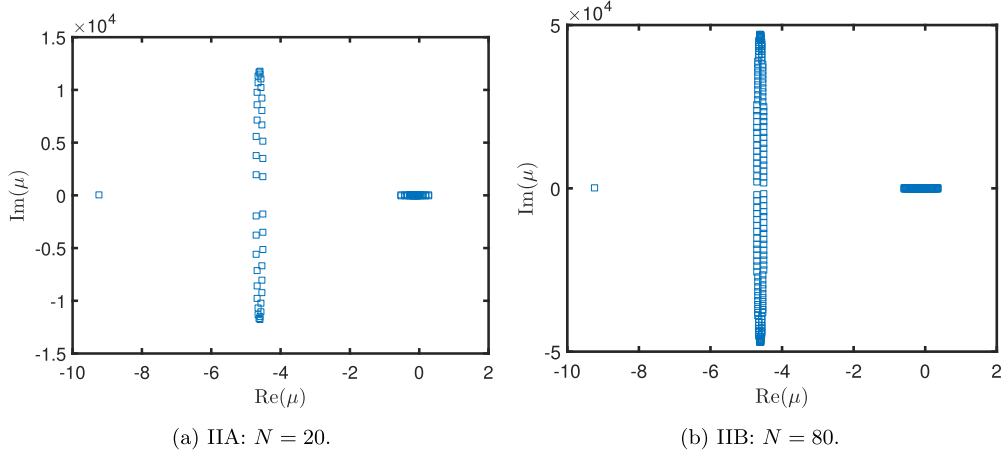


Fig. 6. Case II: grid size effects.

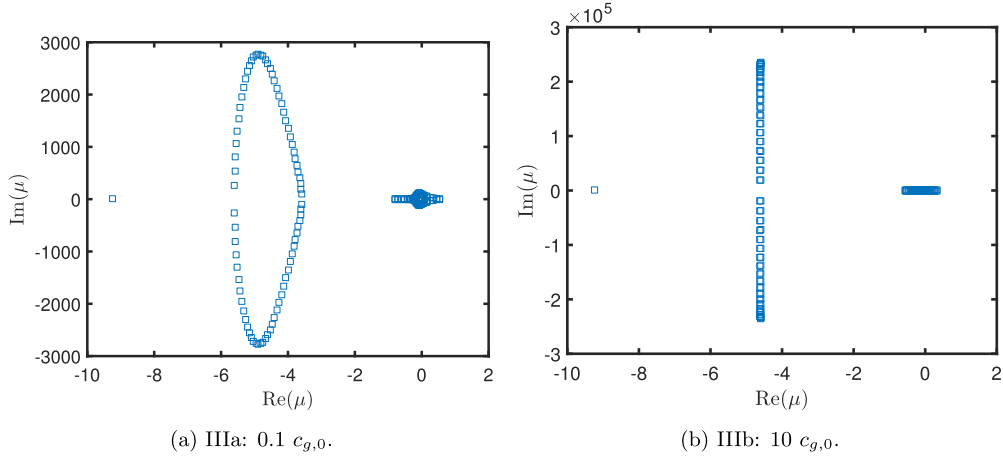


Fig. 7. Case III: compressibility effects.

However, the amount of damping that Crank–Nicolson has on the acoustic modes is not favourable. Consider the largest μ (in absolute sense), then the amplification factors for $\Delta t = 1/40$ s are:

$$G_{\text{exact}} = 0.8914, \quad G_{\text{CN}} = 1.0000, \quad (44)$$

$$G_{\text{BDF2}} = 0.0304, \quad G_{\text{BE}} = 0.00174. \quad (45)$$

Although the amplification factor of Crank–Nicolson is closest to the exact solution (due to its lowest truncation error), it does not possess any damping. At a time step based on the liquid velocity, which in the 1 m long pipe can track the liquid velocity but not the acoustic velocity, the acoustic waves are not resolved and damping is a necessity to prevent unphysical oscillations.

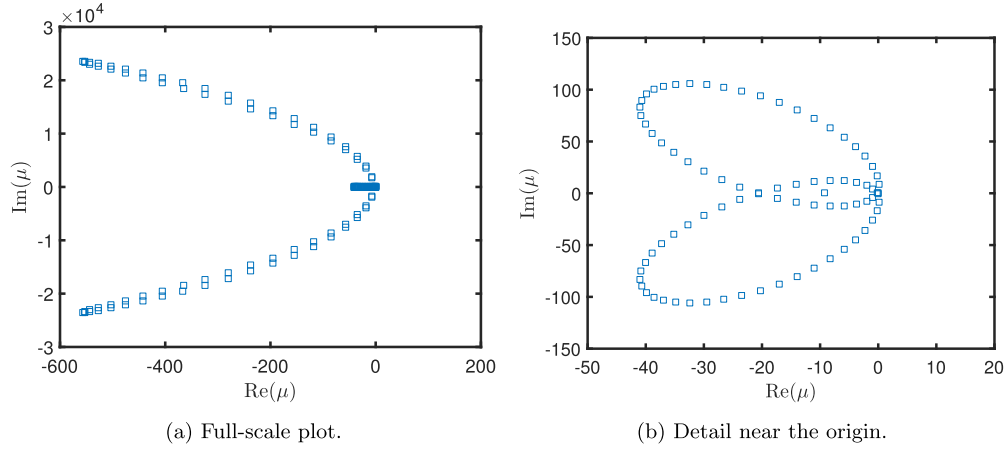


Fig. 8. Eigenvalues for case IV: upwind discretization.

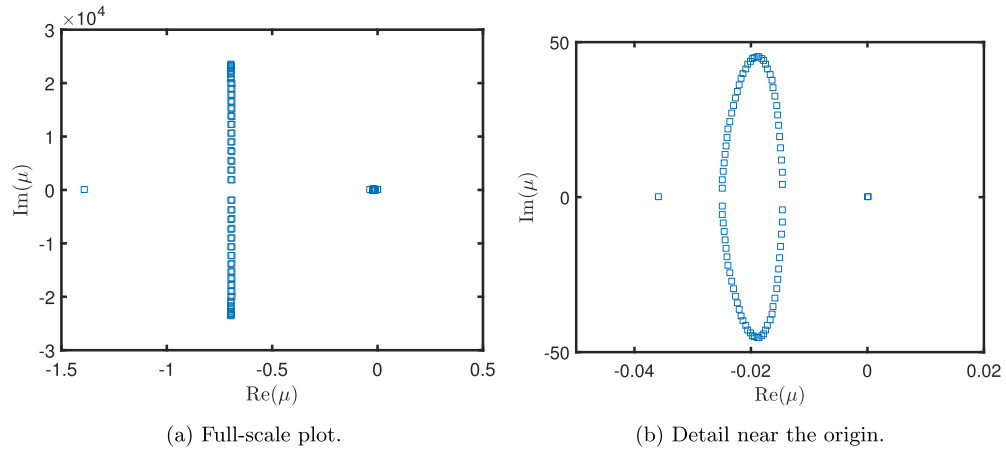


Fig. 9. Eigenvalues for case V: well-posed stable.

5. Von Neumann analysis on the fully discrete equations

5.1. Introduction

In the previous sections the eigenvalues of the continuous and semi-discrete equations were discussed. In the fully discrete case a stability analysis can be performed that is very similar to the one applied to the continuous case (Section 2.3). This is known as von Neumann stability analysis (Morton and Mayers, 2005), which can be seen as the discrete counterpart of the Kelvin–Helmholtz stability analysis (Akselsen, 2016). It is applicable in case of linear, constant coefficient partial differential equations with periodic boundary conditions. We employ therefore the linearized equations (37) in order to be able to apply the von Neumann analysis. As an example, we first consider the equations that result from applying the Backward Euler method:

$$\frac{\tilde{\mathbf{U}}^{n+1} - \tilde{\mathbf{U}}^n}{\Delta t} = \mathbf{J}\tilde{\mathbf{U}}^{n+1}, \quad (46)$$

where $\tilde{\mathbf{U}}$ contains the conservative variables defined on the staggered grid as shown in Fig. 3.

In the von Neumann analysis, which is essentially a discrete Fourier analysis (Morton and Mayers, 2005), the solution is assumed to consist of a finite sum of discrete waves, each with a different wave number:

$$\tilde{\mathbf{U}}_i^n = \sum_m (\mathbf{V}_i^n)_m, \quad (47)$$

$$(\mathbf{V}_i^n)_m = e^{ik_m S_i} \mathbf{v}_m^n = e^{ik_m S_i} \mathbf{G}_m^n \hat{\mathbf{v}}_m, \quad (48)$$

where m indicates the mode number, k_m the wave number of mode m , $\mathbf{G} \in \mathbb{C}^{q \times q}$ the amplification matrix of mode m , and $\hat{\mathbf{v}}_m \in \mathbb{C}^q$ the Fourier coefficients of mode m of the initial condition. $q = 4$ is the dimension of the problem. The fact that we employ an amplification matrix is similar to the approach followed by Fullmer et al. (2014), but slightly different from the scalar amplification factor considered by Liao et al. (2008). We will comment later on the relation between the two. Note that for simplified problems (such as a scalar convection-diffusion equation), the matrix \mathbf{J} is circulant, which means that there is a direct connection between the discrete Fourier transform and the eigendecomposition (38). Unfortunately, the spatially discretized two-fluid model equations do not result in a matrix with circulant structure.

Since Eq. (46) is linear it suffices to consider a single mode $(\mathbf{V}_i^n)_m$ (consisting of solution components at grid points i and $i + 1/2$ due to the staggering) to analyse the stability properties of the discretization method:

$$\begin{pmatrix} V_{1,i} \\ V_{2,i} \\ V_{3,i+1/2} \\ V_{4,i+1/2} \end{pmatrix}_m^{n+1} - \begin{pmatrix} V_{1,i} \\ V_{2,i} \\ V_{3,i+1/2} \\ V_{4,i+1/2} \end{pmatrix}_m^n = \Delta t \sum_{j=1}^N \mathbf{J}_{ij} \begin{pmatrix} V_{1,j} \\ V_{2,j} \\ V_{3,j+1/2} \\ V_{4,j+1/2} \end{pmatrix}_m^{n+1}. \quad (49)$$

Since \mathbf{J} contains the spatial discretization it is very sparse. Substituting the Fourier expansion (48) into Eq. (49), omitting the subscript m , and dividing each equation by the complex exponential

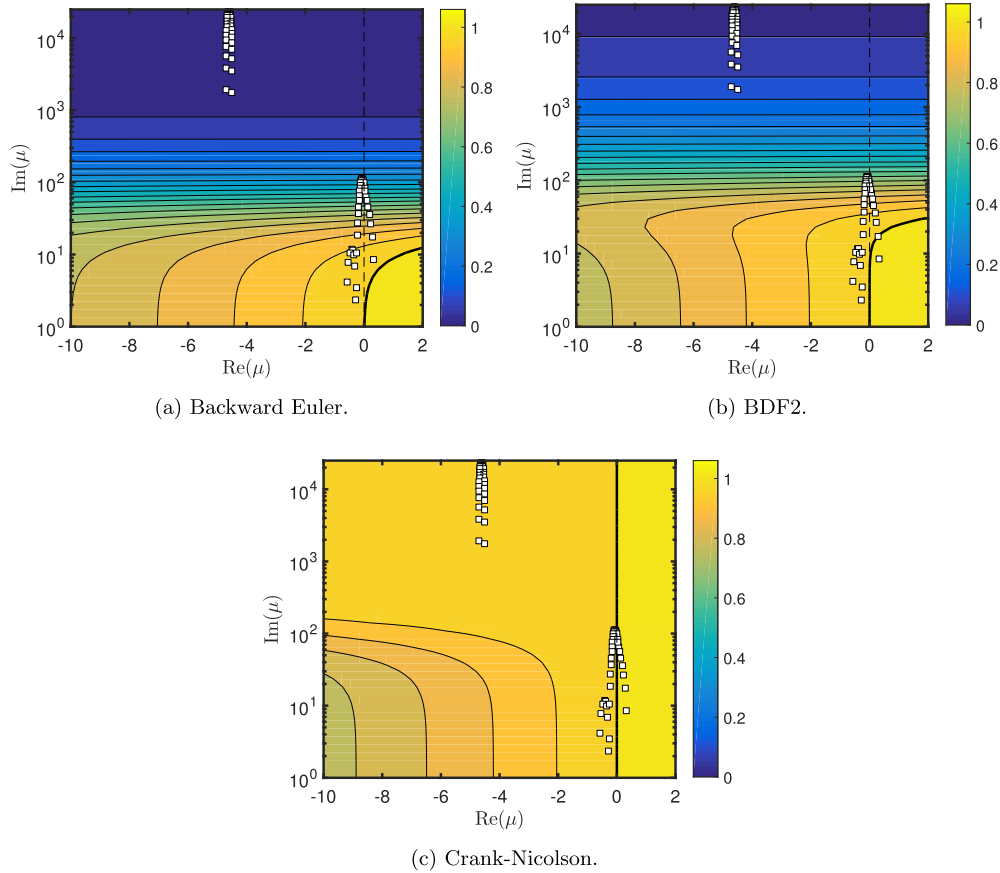


Fig. 10. Amplification factor G for different time integration methods when superimposed on the eigenvalues of Fig. 4. Contour lines are 0.05 apart; thick black lines indicate $G = 1$.

in space, yields the compact expression

$$\begin{pmatrix} v_{1,i} \\ v_{2,i} \\ v_{3,i+1/2} \\ v_{4,i+1/2} \end{pmatrix}^{n+1} - \begin{pmatrix} v_{1,i} \\ v_{2,i} \\ v_{3,i+1/2} \\ v_{4,i+1/2} \end{pmatrix}^n = \Delta t \mathbf{M}(e^{lk_m s_i}) \begin{pmatrix} v_{1,i} \\ v_{2,i} \\ v_{3,i+1/2} \\ v_{4,i+1/2} \end{pmatrix}^n. \quad (50)$$

Eq. (50) is useful in a fully analytical point approach, whereas Eq. (49) is the equation that can be used when performing symbolic operations in our coding environment. The notation $\mathbf{M}(e^{lk_m s_i})$ indicates the action of the spatial discretization on a complex exponential and is called the discrete Fourier symbol; it follows when substituting a discrete exponential in the discretization method and subsequently dividing it by this discrete exponential. For example, if a central discretization is used for the convective term in the mass equation for the gas, i.e.

$$V_{1,i}^{n+1} - V_{1,i}^n = -\Delta t \frac{V_{3,i+1/2}^{n+1} - V_{3,i-1/2}^{n+1}}{\Delta s}, \quad (51)$$

then the Fourier representation is

$$v_{1,i}^{n+1} - v_{1,i}^n = -\Delta t \frac{v_3^{n+1} e^{lk_m s_{i+1/2}} - v_3^{n+1} e^{lk_m s_{i-1/2}}}{e^{lk_m s_i} \Delta s}, \quad (52)$$

and the matrix entry is

$$\mathbf{M}_{1,3} = -\frac{l \sin(k_m \Delta s/2)}{\Delta s/2}. \quad (53)$$

The full matrix is similar to the one presented by Liao et al. (2008), but much more elaborate due to the fact that we employ a 4×4 system including compressibility effects. In Section 5.3 a method will be proposed which circumvents the explicit formulation of

this matrix. We write Eq. (50) in the following generic form, using a notation similar to Fullmer et al. (2014):

$$\mathbf{N} \mathbf{v}^{n+1} = \mathbf{O} \mathbf{v}^n, \quad \text{or} \quad \mathbf{v}^{n+1} = \mathbf{N}^{-1} \mathbf{O} \mathbf{v}^n, \quad (54)$$

where for Backward Euler: $\mathbf{N} = \mathbf{I} - \Delta t \mathbf{M}$, and $\mathbf{O} = \mathbf{I}$. The amplification matrix is given by

$$\mathbf{G} = \mathbf{N}^{-1} \mathbf{O}. \quad (55)$$

Stability depends on the spectral radius of \mathbf{G} , i.e. the maximum absolute value of the (complex) eigenvalues λ_G of \mathbf{G} . These eigenvalues λ_G follow from the eigenvalue problem

$$\det(\mathbf{N} \lambda_G - \mathbf{O}) = 0, \quad (56)$$

and a scalar amplification factor can be defined as $G = \max_i |\lambda_{G,i}|$. The amplification matrix \mathbf{G} is the one used by Fullmer et al. (2014), whereas the amplification factor λ_G is used by Liao et al. (2008). \mathbf{G} contains the growth and frequency components of all waves, which allows the reconstruction of the full solution, which is not possible with λ_G . In Section 5.3 we will obtain the amplification factors from simulation data only, and this requires the use of the full \mathbf{G} .

Once the amplification matrix \mathbf{G} and the Fourier coefficients \mathbf{v} of the initial condition are known, the solution at a time instance t^n in terms of Fourier coefficients is obtained from

$$\mathbf{v}_m^n = \mathbf{G}_m^n \hat{\mathbf{v}}_m, \quad \text{or} \quad \mathbf{v}_m^{n+1} = \mathbf{G}_m \mathbf{v}_m^n. \quad (57)$$

\mathbf{G} contains information about the *growth* of the solution (diffusive errors), and about the *shift* (dispersive errors) of the solution in time.

5.2. Extension to BDF2 and Crank–Nicolson

For the BDF2 scheme, Eq. (50) becomes

$$\mathbf{N}\mathbf{v}^{n+1} + \mathbf{O}\mathbf{v}^n + \mathbf{P}\mathbf{v}^{n-1} = 0, \quad (58)$$

where $\mathbf{N} = a_0\mathbf{I} - \Delta t\mathbf{M}$, $\mathbf{O} = a_1\mathbf{I}$, $\mathbf{P} = a_2\mathbf{I}$. This equation can be written as

$$\begin{pmatrix} a_0\mathbf{I} - \Delta t\mathbf{M} & 0 \\ 0 & \mathbf{I} \end{pmatrix} \begin{pmatrix} \mathbf{v}^{n+1} \\ \mathbf{v}^n \end{pmatrix} = \begin{pmatrix} -a_1\mathbf{I} & -a_2\mathbf{I} \\ \mathbf{I} & 0 \end{pmatrix} \begin{pmatrix} \mathbf{v}^n \\ \mathbf{v}^{n-1} \end{pmatrix},$$

or:

$$\hat{\mathbf{N}}\mathbf{w}^{n+1} = \hat{\mathbf{O}}\mathbf{w}^n, \quad (59)$$

from which the definition of \mathbf{G} follows:

$$\mathbf{G} = \hat{\mathbf{N}}^{-1}\hat{\mathbf{O}} = \begin{pmatrix} -a_1(a_0\mathbf{I} + \mathbf{M})^{-1} & -a_2(a_0\mathbf{I} + \mathbf{M})^{-1} \\ \mathbf{I} & 0 \end{pmatrix}. \quad (60)$$

This is a particular case of the more generic linear multistep methods analysed in [Hundsdoerfer and Verwer \(2007\)](#). The eigenvalues of \mathbf{G} follow from the determinant equation

$$\det(\hat{\mathbf{N}}\lambda_G - \hat{\mathbf{O}}) = \det((a_0\mathbf{I} - \Delta t\mathbf{M})\lambda_G^2 + a_1\lambda_G\mathbf{I} + a_2\mathbf{I}) = 0. \quad (61)$$

Note the similarity with the scalar amplification Eq. (43). When including the Crank–Nicolson method this can be generalized to

$$\det\left(\frac{a_0 + a_1G^{-1} + a_2G^{-2}}{\Delta t}\mathbf{I} - (\theta\mathbf{M} + (1-\theta)\mathbf{M}G^{-1})\right) = 0, \quad (62)$$

where we write G instead of λ_G .

5.3. Amplification factor from simulation data

In this section we propose an alternative, novel method to obtain the von Neumann amplification factors without the need of doing symbolic manipulations, as this can be cumbersome for non-linear models with elaborate closure relations, such as in the case of the two-fluid model. The idea is to perform a simulation with a small-amplitude harmonic as initial condition and to derive the amplification matrix by comparing the Fourier transform of the solution at a certain time level to the Fourier transform of solutions at previous time levels. We call this the *automatic* von Neumann analysis, in contrast to the classical *symbolic* von Neumann analysis that uses symbolic manipulations. First, the Fourier coefficients \mathbf{v}_m of mode m are determined from the numerical solution \mathbf{V} by a discrete Fourier transform, similar to Eq. (48):

$$\mathbf{v}_m^n = \sum_i \mathbf{V}_i^n e^{ik_m s_i} \Delta s_i. \quad (63)$$

Given the solutions \mathbf{v}^{n+1} and \mathbf{v}^n , the coefficients of the matrix cannot be determined from (57), since we have q equations for q^2 unknowns. We therefore perform q time steps and write

$$\begin{pmatrix} \mathbf{v}_m^{n+1} & \mathbf{v}_m^n & \dots & \mathbf{v}_m^{n+2-q} \end{pmatrix} = \tilde{\mathbf{G}}_m \begin{pmatrix} \mathbf{v}_m^n & \mathbf{v}_m^{n-1} & \dots & \mathbf{v}_m^{n+1-q} \end{pmatrix}, \quad (64)$$

or

$$\mathbf{Q}_m^{n+1} = \tilde{\mathbf{G}}_m \mathbf{Q}_m^n, \quad (65)$$

from which the matrix $\tilde{\mathbf{G}}_m$ can be readily determined:

$$\tilde{\mathbf{G}}_m = \mathbf{Q}_m^{n+1} (\mathbf{Q}_m^n)^{-1}. \quad (66)$$

We write $\tilde{\mathbf{G}}$ instead of \mathbf{G} to distinguish between the symbolic and the automatic von Neumann analysis. For the BDF2 scheme, $\tilde{\mathbf{G}} \in \mathbb{C}^{2q \times 2q}$, and the system of equations is extended to

$$\begin{pmatrix} \mathbf{v}_m^{n+1} & \mathbf{v}_m^n & \dots & \mathbf{v}_m^{n+2-2q} \\ \mathbf{v}_m^n & \mathbf{v}_m^{n-1} & \dots & \mathbf{v}_m^{n+1-2q} \\ \mathbf{v}_m^{n-1} & \mathbf{v}_m^{n-2} & \dots & \mathbf{v}_m^{n-2q} \end{pmatrix} = \tilde{\mathbf{G}}_m \begin{pmatrix} \mathbf{v}_m^n & \mathbf{v}_m^{n-1} & \dots & \mathbf{v}_m^{n+1-2q} \\ \mathbf{v}_m^{n-1} & \mathbf{v}_m^{n-2} & \dots & \mathbf{v}_m^{n-2q} \end{pmatrix}. \quad (67)$$

In order to construct \mathbf{Q}_m^{n+1} and \mathbf{Q}_m^n , it suffices to take $2q$ time steps and to store the Fourier coefficients at each time step (of course, one can also store the entire solution and calculate the Fourier coefficients afterwards). Once $\tilde{\mathbf{G}}$ is determined, the absolute value of its eigenvalues can be investigated. This has to be done for all wavenumbers, either by rerunning the simulation with an initial condition for each different wave, or performing one simulation with a single initial condition composed of all wavenumbers. This is a simple and fast procedure given that only $2q = 8$ time steps are necessary to reconstruct $\tilde{\mathbf{G}}$. In practice, we have noted that due to the high condition number of \mathbf{Q}^n inaccurate results are sometimes obtained. This can be resolved by increasing the number of time instances in the analysis to for example $4q$, which works well in our simulations. The matrices \mathbf{Q}^n and \mathbf{Q}^{n+1} then become non-square and the solution of (67) should be interpreted in a least-squares sense.

To summarize, in this section we have explained two techniques, symbolic and automatic von Neumann analysis. This will be demonstrated for the Kelvin–Helmholtz instability case in [Section 6.1](#). The first is the classic analysis: substitution of a Fourier series in the discretization matrix and investigating the resulting amplification matrix and its eigenvalues. We have done this by using the symbolic toolbox of Matlab and by direct substitution of the complex exponentials into our code to arrive at symbolic expressions for the amplification matrix. The second technique is based on substituting sinusoidal wave perturbations in the initial conditions, and running the code for several time steps. This can be used to check the outcome of the first technique, but also to obtain amplification matrices for black-box solvers (for instance commercial codes).

6. Results for various test cases

In this section we report the results of four test cases. The first three are related to the Kelvin–Helmholtz instability; the first one considers steady state flow with a small but unstable perturbation in a single wave to validate the linear stability (von Neumann) and accuracy of the time integration methods. The second case considers the same instability but with a much larger perturbation to study the nonlinear wave growth and the identification of ill-posedness. The third case considers stiffness by including perturbations in both the convective and acoustic waves, and we investigate how the time integrators resolve the acoustics. Lastly, in the fourth test case the propagation of a hold-up wave is investigated, and all the previously investigated concepts of stability, accuracy, ill-posedness and resolution of acoustics are considered. The four cases will be referred to as A, B, C, and D, respectively.

6.1. Kelvin–Helmholtz: Linear wave growth

6.1.1. Modified wave number analysis

We consider the Kelvin–Helmholtz instability for the test problem described in Section 2.4 and with the conditions given in Table 1. The exact solution to the linearized system of equations (19) is given by

$$\mathbf{W}(s, t) = \mathbf{W}_0 + \sum_j \text{Re} [\mathbf{e}_j e^{I(\omega_j t - ks)}]. \quad (68)$$

The initial condition is obtained by a small perturbation in the liquid hold-up: $\tilde{\alpha}_l = 10^{-6}$. The perturbation vector \mathbf{e}_3 is taken to be the eigenvector associated to the angular frequency ω_3 (Liao et al., 2008):

$$\mathbf{e}_3 = 10^{-4} \begin{pmatrix} 1 \cdot 10^{-2} \\ 7.005 \cdot 10^{-3} - 1.1025 \cdot 10^{-3}I \\ 2.497 \cdot 10^{-1} + 1.186 \cdot 10^{-3}I \\ -3.619 - 6.550 \cdot 10^{-1}I \end{pmatrix}. \quad (69)$$

First we perform a consistency check: simultaneous grid and time step refinement for a fixed wave number $k = 2\pi$ with

$$C_l \approx 1 \rightarrow \Delta t \approx \Delta s = \frac{1}{N}, \quad (70)$$

where C is the dimensionless time step, similar to the CFL number (which strictly is a stability condition). $k = 2\pi$ is the smallest wave number that can be presented on our periodic simulation domain. The exact growth rate, $\text{Im}(\omega_3) = -0.35$, is compared to the numerically computed growth rates as obtained from the symbolic and the automatic von Neumann analysis:

$$\omega_{vN} = \frac{\ln(\min(\text{Im}(\lambda(\mathbf{G}_m))))}{\Delta t}, \quad \tilde{\omega}_{vN} = \frac{\ln(\min(\text{Im}(\lambda(\tilde{\mathbf{G}}_m))))}{\Delta t}. \quad (71)$$

Even though only a single wave is triggered due to the initial perturbation in \mathbf{e}_3 , the discrete amplification matrix \mathbf{G} still has four eigenvalues. This is because the Fourier transform of the initial condition does not consist of a single wave, but of four waves. We are interested in the one that is largest in magnitude, since it indicates whether the numerical solution is stable or not. However, in contrast to the classical von Neumann analysis, in this study unstable solutions are not necessarily unwanted, since the differential equation itself has an unstable behaviour (Fullmer et al., 2014), which might be associated to slug flow.

Fig. 11 shows the comparison of ω_3 to ω_{vN} and $\tilde{\omega}_{vN}$, for different grids and discretization schemes. Fig. 11a shows that all time discretization methods converge to the exact growth rate upon grid refinement. However, for coarse grids, the Backward Euler method predicts a positive ω (damped solutions), whereas BDF2 and Crank–Nicolson correctly predict growing solutions (albeit with a reduced growth rate). In Fig. 11b this is made more quantitative by computing the error of the discrete models compared to the exact value:

$$\eta = |\omega_3 - \omega_{vN}|. \quad (72)$$

It is clear that the use of Backward Euler or the use of the first order upwind scheme limits the accuracy to first order. Fig. 11b also indicates that for very fine meshes there is a slight discrepancy between the symbolic and automatic von Neumann analysis. This is related to the matrix inversion required for the reconstruction (66) in the automatic von Neumann analysis, which can suffer from numerical inaccuracies. For the main purpose of the von Neumann analysis, namely investigating the behaviour of the numerical growth rate or dispersion error as function of phase angle ($\phi = k\Delta s$), this is not an issue.

Secondly, we investigate how waves grow in time, depending on the wave number k and the spatial and temporal discretization. The number of grid points is fixed ($\Delta s = 1/160$ m). The shortest wavelength that can be represented on the grid is $2\Delta s$ (Nyquist limit), corresponding to the wavenumber $k = \pi/\Delta s$, and phase angle $\phi = \pi$. The wave number analysis provides insight into how well waves of different frequency are resolved by the time integration method. It is similar to the analysis for spatial discretization methods done by Liao et al. (2008). Fig. 12a shows the growth rate $G = \max|\lambda(\mathbf{G})|$ which compares well with the results of Liao et al. (2008). In addition, Fig. 12b shows the growth rate ω_{vN} instead of the amplification factor, which includes the exact solution (denoted by the black dashed line). This line corresponds to the dashed line previously shown in Fig. 2b. It is perhaps not surprising to see that Crank–Nicolson (‘central in time’) with a central scheme in space leads to an accurate prediction of G . In fact, when performing the analysis without friction terms (in the well-posed stable regime), the Crank–Nicolson / central combination leads to $G = 1$ independent of the wavenumber. This is a well-known result for advection equations and also holds for the two-fluid model without source terms. However, the presence of source terms leads to unstable solutions; their growth rate can be captured by the numerical scheme though, with the accuracy of the time integration method. Furthermore, $G = 1$ does not mean that the numerical is exact, but that there are only dispersive errors and no diffusive errors.

For each wavenumber k the corresponding growth rate ω_3 is negative. This agrees with the stability-hyperbolicity theorem (Prosperetti and Tryggvason, 2007) which says that the neutral stability limit is independent of the wavenumber. The case of $k = 2\pi$ from Fig. 11 is highlighted as the black vertical line in Fig. 12. For $\phi < 10^{-2}$ all numerical methods perform well - this corresponds to long, low frequency waves which are well resolved. For larger ϕ the numerical damping of all methods becomes apparent. The kinks in the amplification factor and the growth rate are due to the fact that a different eigenvalue (see Eq. (71)) becomes dominant.

6.1.2. Linearized discrete flow pattern map prediction

In this section we propose a novel way for displaying the performance of numerical methods, which we call ‘Discrete Flow Pattern Maps’ (DFPM), that uses the growth rate determination method developed for the automatic von Neumann analysis (Eq. (66)). Whereas traditional flow pattern maps, such as the one in Fig. 1, display stable and unstable regimes based on the properties of the differential equations, the DFPM displays the effective stability regions that result when the discrete equations are solved, with a certain numerical method and a certain grid and time resolution. Such a map is of crucial importance as an indication whether a discretization method is able to correctly capture the well-posed unstable regime (and the potential transition to slug flow) or whether numerical diffusion overwhelms the physical growth of instabilities.

The DFPM can be constructed in the same way in which we constructed the flow pattern map in Fig. 1. We employ a sequence of superficial liquid and gas velocities, solve the discrete equations with a small perturbation as initial condition and determine the growth rate $\tilde{\omega}_{vN}$ from (66) and (71). The stability boundary is given by $\text{Im}(\tilde{\omega}_{vN}) = 0$. Fig. 13a shows the VKH stability boundary for Backward Euler and BDF2 for two different grids (and associated time steps). It can be seen that BDF2 captures the exact stability boundary very accurately on all grids. On the other hand, the effective stability region given by Backward Euler is much larger (note the log scale) than the actual stability region of the differential equations, due to the large amount of artificial diffusion added by Backward Euler. For example, for $N = 40$, and at a superficial

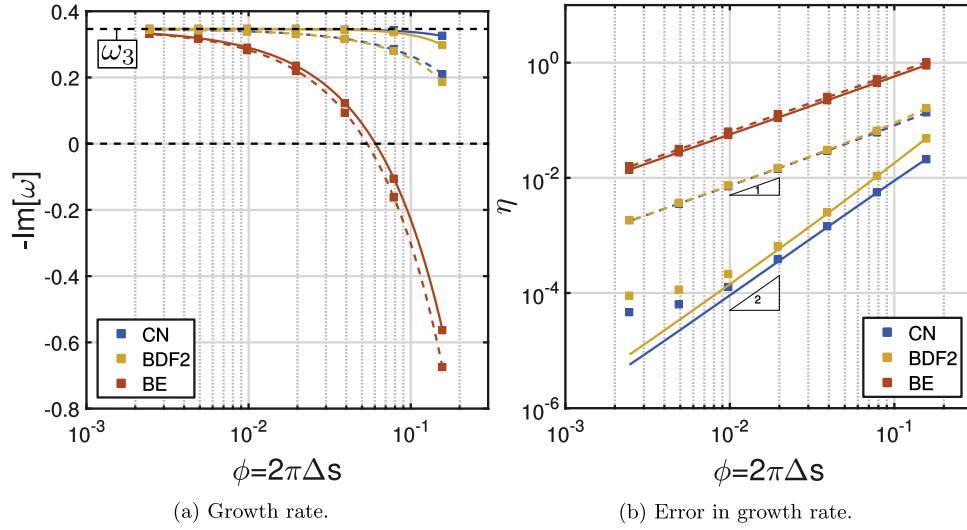


Fig. 11. Comparison of the growth rate and the error in the growth rate for different discretization methods as a function of the grid size. Squares: automatic von Neumann analysis, lines: symbolic von Neumann analysis. Dashed lines: first order upwind, solid lines: second order central.

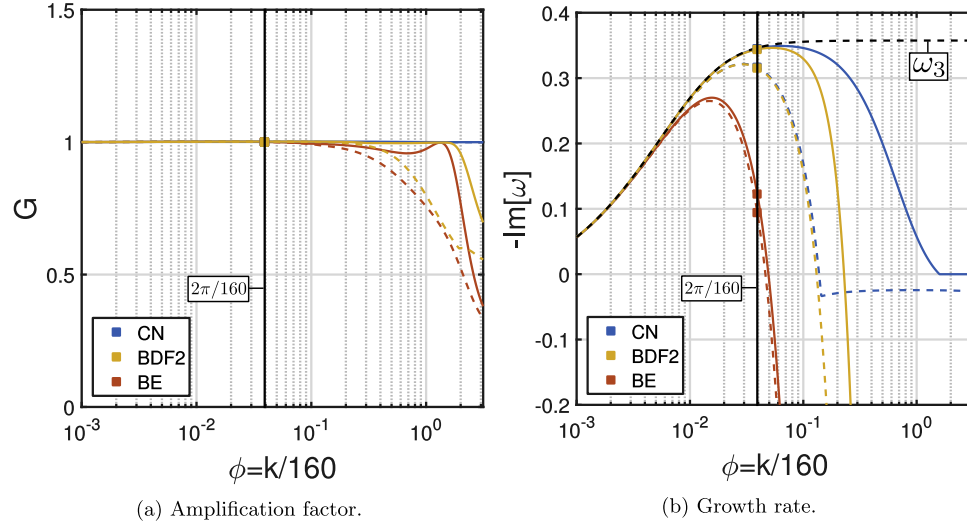


Fig. 12. Comparison of the growth rate and the error in the growth rate for different discretization methods as a function of the wave number. Dashed lines: first order upwind, solid lines: second order central.

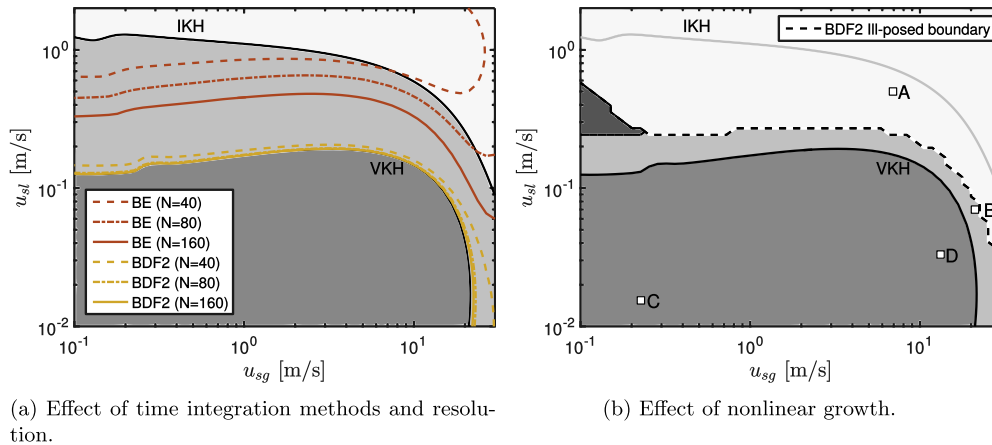


Fig. 13. Discrete flow pattern maps (DFPM).

gas velocity of $u_{sg} = 10$ m/s, the two-fluid model predicts growing waves at a superficial liquid velocity of $u_{sl} = 0.15$ m/s, but with Backward Euler the wave growth is only apparent when the superficial liquid is increased to $u_{sl} = 0.6$ m/s (already at the ill-posed boundary).

Any simulation starting above the ill-posedness boundary will directly be marked as ill-posed, because our ill-posedness indicator is based on the evaluation of the eigenvalues of the differential equations, see Eq. (12). However, it is possible that, due to nonlinear effects, simulations that start in the well-posed unstable regime grow into the ill-posed regime. This is investigated in the next section.

6.2. Kelvin–Helmholtz: Nonlinear wave growth

In this section the simulation from Section 6.1 is repeated, but with a larger perturbation: $\tilde{\alpha}_l = 10^{-2}$, and $\tilde{\epsilon}_3 = 10^4 \epsilon_3$. This causes the simulation to quickly enter the nonlinear regime, in which waves steepen, possibly leading to slug formation but potentially also to ill-posedness. Based on the results of the previous section, we select BDF2 with $N = 80$ to assess the growth of initial perturbations into the nonlinear regime and whether this leads to ill-posed results. Note that this is different from a previous paper (Hendrix et al., 2016), in which we have assessed the ‘time to ill-posedness’ as a metric to compare different time integration methods. In the present study the focus is on whether well-posed unstable solutions can be obtained for long time integration periods.

Similar to the linear case, we perform simulations with the two-fluid model with a central discretization for a range of superficial gas and liquid velocities but now until $t = 100$ s and only with a central discretization of the convective terms. Ill-posedness is investigated by checking if the eigenvalues of the differential equations are real or complex at the conditions predicted by the numerical simulation. If a complex eigenvalue occurs at any point in space or time the corresponding point in the flow pattern map is marked ill-posed. Fig. 13b shows that the resulting numerical ill-posedness boundary has shifted significantly into the well-posed unstable regime as compared to the ill-posedness boundary of the differential equations (indicated by IKH in Fig. 13b). It appears that a large part of the well-posed unstable regime of the flow pattern map gives ill-posed solutions when actual numerical simulations are performed. An example of a simulation which turns ill-posed is case A in Fig. 13b, which corresponds to the conditions studied in Section 6.1 for linear perturbations. The nonlinear behaviour of the hold-up fraction α_l in space and time is shown in Fig. 14 for this case. The solution becomes ill-posed already after approximately 5 s. The liquid hold-up fraction as a function of time at $s = 1$ m is shown in Fig. 15a.

In addition to case A, three other cases (B, C, and D) are indicated in Fig. 13b which exhibit qualitatively different solution behaviour. Case B in Fig. 15b starts in the well-posed unstable regime, like case A, but after initial growth (as predicted by linear theory) stabilizes and forms a wave with a constant amplitude and frequency. Its shape and position in the flow pattern map indicate that this could be a so-called continuous ‘roll wave’: a particular solution to the two-fluid model which is constant in a reference frame moving with the flow (Barnea and Taitel, 1993; Holmås, 2010; Johnson, 2005). To check that this is not a numerical artefact, we have confirmed the roll wave presence with a simulation on a much finer grid ($N = 640$). Case C and D are both in the well-posed stable regime, where initial perturbations are damped according to the linear theory. This happens indeed for case D. However, for case C, the damping is very small ($\text{Im}(\omega_3) = 0.01$) and nonlinear effects lead to wave growth and the appearance of new harmonics. The oscillation frequency is now lower because the real part of ω_3 has decreased. Within the time period of 100 s displayed in the

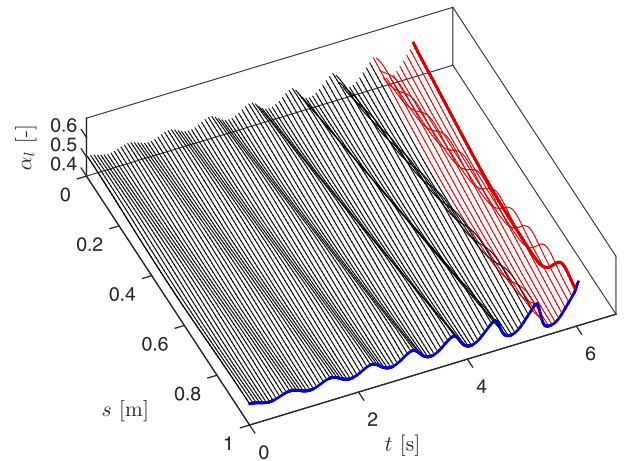


Fig. 14. Solution in space and time for case A, simulated with BDF2: well-posed unstable solution becoming ill-posed (indicated in red). The blue curve is shown in Fig. 15a. (For interpretation of the references to colour in this figure legend, the reader is referred to the web version of this article.)

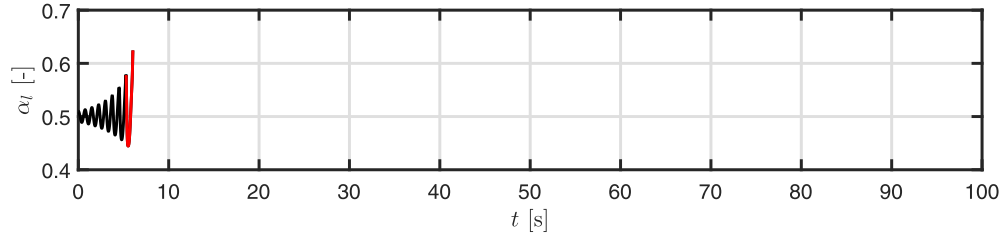
plot it is unclear if the wave damps out. Continued simulation until 1000 s reveals that the wave eventually damps out, like in case D.

We note that the current simulation results are obtained based on a number of simplifications compared to pipeline simulations on actual geometries. First, we employed initial perturbations according to the eigenvector ϵ_3 . This means that the perturbations immediately grow according to linear theory until nonlinear effects take over. Second, we used a single wave with wavenumber $k = 2\pi$. Other wavenumbers will have different frequencies and growth rates and can lead to qualitatively different behaviour (although the VKH and IKH boundaries are independent of wavenumber). Furthermore, the periodic boundary conditions and size of the domain limit the frequencies that can be represented on the domain. Lastly, we note the black region in Fig. 13b, which indicates the region where the liquid reaches the top of the pipeline. This is not necessarily ill-posed, but outside the scope of our investigation.

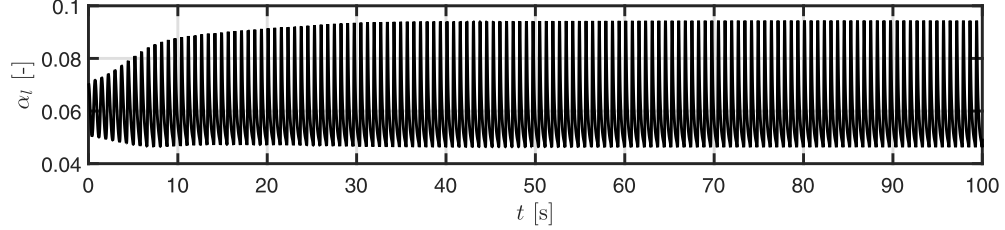
6.3. Kelvin–Helmholtz: Acoustic wave problem

In this test the Kelvin–Helmholtz instability problem from Section 6.2 is extended to take into account acoustic waves, which were not present in previous studies (e.g. Fullmer et al., 2014; Liao et al., 2008) as these used the incompressibility assumption. We propose this acoustic wave problem as test case for pipeline simulation codes that solve the compressible two-fluid model. In order to demonstrate the acoustic filtering capabilities of BDF2 we choose two waves (see Eq. (23)): (i) a slow, right moving, unstable (growing) wave with frequency $\omega_3 = 8.48 - 0.35I$, and (ii) a fast, left moving, stable (damped) wave with frequency $\omega_1 = -1758.05 + 4.51I$. This extends Section 6.1 where only a single wave was considered. The hold-up fraction for the slow wave is again 10^{-6} , whereas the hold-up fraction for the fast wave is 10^{-2} . As before, the perturbations ϵ_1 and ϵ_3 are taken as the eigenvectors that follow from the dispersion analysis:

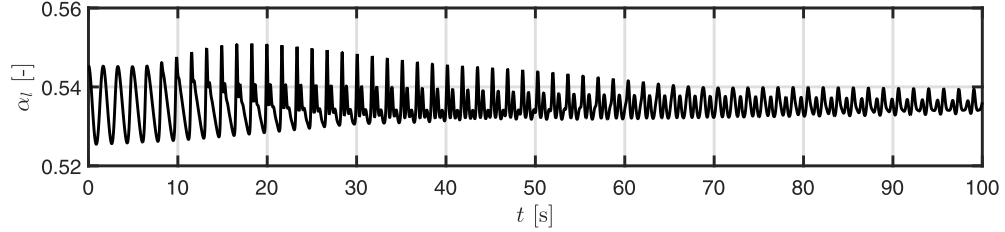
$$\epsilon_1 = \begin{pmatrix} 1 \cdot 10^{-6} \\ -5.616 \cdot 10^{-4} + 1.435 \cdot 10^{-6}I \\ -4.624 \cdot 10^{-1} + 4.876 \cdot 10^{-3}I \\ 1.577 \cdot 10^2 - 1.276I \end{pmatrix},$$



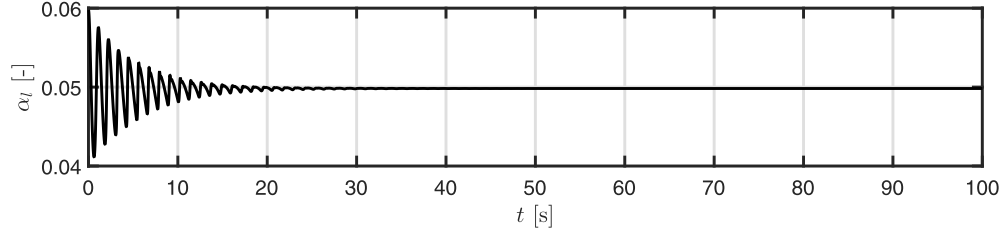
(a) Case A: Well-posed unstable solution turns ill-posed. $u_{sg} = 6.91$ m/s, $u_{sl} = 0.5$ m/s, $\omega_3 = 8.48 - 0.35I$.



(b) Case B: Well-posed unstable solution becomes stationary (roll waves). $u_{sg} = 21.16$ m/s, $u_{sl} = 0.07$ m/s, $\omega_3 = 8.32 - 0.14I$.



(c) Case C: Well-posed stable solution grows, encounters nonlinear effects and then damps. $u_{sg} = 0.23$ m/s, $u_{sl} = 0.015$ m/s, $\omega_3 = 3.73 + 0.01I$.



(d) Case D: Well-posed stable solution damps in time. $u_{sg} = 13.28$ m/s, $u_{sl} = 0.033$ m/s, $\omega_3 = 5.35 + 0.18I$.

Fig. 15. Numerical solutions for cases A–D as indicated in Fig. 13b, simulated using BDF2.

$$\mathbf{e}_3 = \begin{pmatrix} 1 \cdot 10^{-2} \\ 7.005 \cdot 10^{-3} - 1.1025 \cdot 10^{-3}I \\ 2.497 \cdot 10^{-1} + 1.186 \cdot 10^{-3}I \\ -3.619 - 6.550 \cdot 10^{-1}I \end{pmatrix}. \quad (73)$$

The particular choice for hold-up fractions leads to the following combined wave system:

- A slow, right moving, growing liquid hold-up fraction wave.
- A fast, left moving, pressure wave, which is damped in time, so that after long periods a slow, right moving, growing pressure wave becomes dominant.
- A slow, right moving, growing wave in the liquid velocity, perturbed by a smaller amplitude, fast left moving wave, which is damped out.
- A fast, left moving, damped wave in the gas velocity, perturbed by a smaller amplitude, slow right-moving, growing wave, which becomes dominant for long periods.

A qualitative impression of the behaviour of the numerical solution for short and long time periods, for different integration meth-

ods, is given in Figs. 16–18. A central scheme has been used to discretize the convective terms. The short time scale is closely related to the speed of sound in the gas and we define a dimensionless time step of $\frac{1}{2}$ based on this time scale:

$$C_c = \frac{1}{2} \rightarrow \Delta t = \frac{1}{2} \frac{\Delta s}{c_g} \approx 4.26 \cdot 10^{-5} \text{ s}, \quad t_{\text{end},c} = 400 \Delta t \approx 0.017 \text{ s}. \quad (74)$$

The long time period is based on the initial liquid velocity, and we define a dimensionless time step and end time based on this time scale:

$$C_l = 1 \rightarrow \Delta t = \frac{\Delta s}{u_l} = 0.025 \text{ s}, \quad t_{\text{end},l} = 0.25 \text{ s}. \quad (75)$$

Note that the gas velocity is around 14 m/s, which gives a dimensionless time step based on the gas velocity of approximately 14.

First, we investigate the resolution of the acoustic waves on the short time scale. Fig. 16 displays the solution obtained with BDF2 until $t_{\text{end},c}$. The liquid hold-up fraction α_l clearly shows the slow

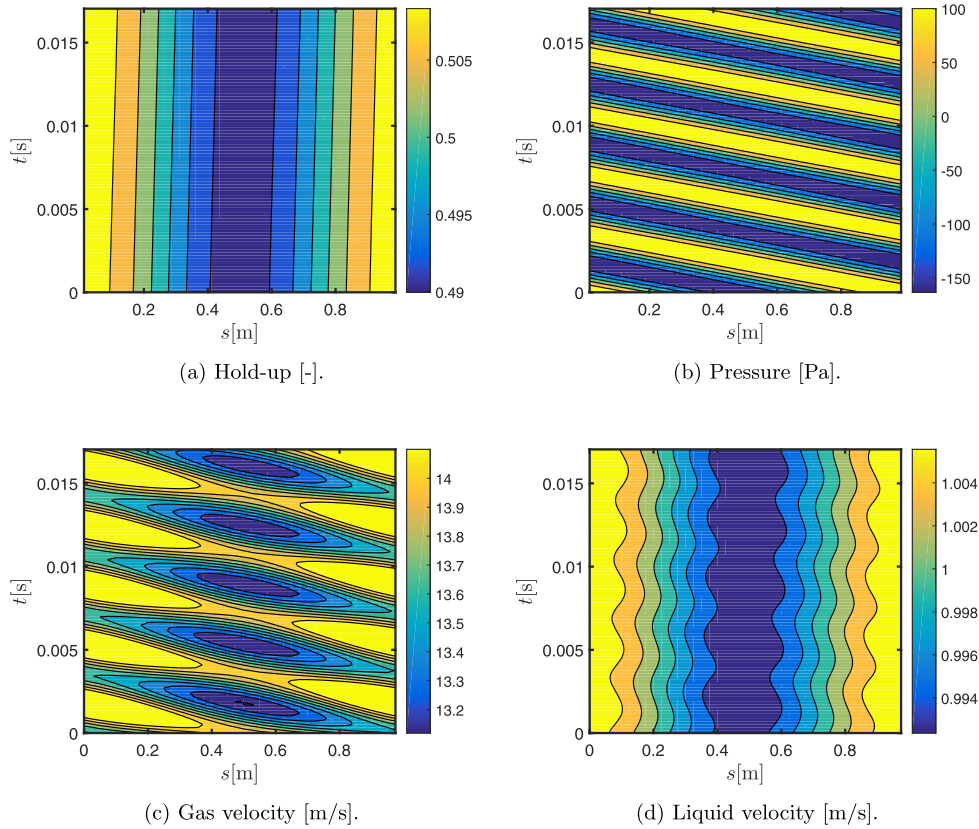


Fig. 16. Solution of acoustic wave problem in $s - t$ diagrams. BDF2, $C_c=0.5$.

right moving wave associated with ω_3 . The pressure, on the other hand, displays the fast wave moving to the left. The liquid and gas velocity show predominantly the left and right moving wave, respectively, but with perturbations in the other wave. The solution is quantitatively the same as the solutions obtained with the Crank–Nicolson scheme and with the Runge–Kutta method (reference solution) at this $C_c = \frac{1}{2}$: both BDF2 and Crank–Nicolson are well able to resolve acoustic waves at a time step based on the speed of sound in the gas.

Secondly, we increase the time step and take $C_l = 1$, which is common in many practical computations in which the accurate resolution of acoustic waves is not important. Fig. 17 shows that BDF2 effectively kills the acoustic waves during the first time steps, and only the hold-up wave remains. This corresponds to the amplification factor (45) and the results in Fig. 10b. On the other hand, Fig. 18 shows that when Crank–Nicolson is employed with this increased time step, a non-physical oscillation in the pressure appears which is not damped in time. This oscillation also becomes apparent in the gas velocity and to a lesser extent in the liquid velocity. The hold-up wave is hardly affected. Therefore, although Crank–Nicolson gives stable results (it is an A -stable method), it does not damp out unresolved transients (it is not L -stable). This confirms the results from Eq. (44) and in Fig. 10c.

Fig. 19 compares the results for different time integration methods in a single plot at $t = 1$ s and $C_l = 1$. The reference solution has been obtained with the explicit Runge–Kutta method with $C_c = 0.5$ and its temporal error can be considered negligible. The BDF2 and CN schemes are both giving an accurate prediction for the liquid hold-up fraction and the liquid velocity. However, in both the pressure and the gas velocity, the prediction of Crank–Nicolson is very far off. This renders the Crank–Nicolson scheme essentially useless in these situations. Slightly increasing the value of θ (for example

to 0.55), will improve the long time behaviour since some damping is introduced. However, this does not work on short time scales, and comes at a price of reduced accuracy. Backward Euler does not suffer from oscillations, though it has severely damped the amplitude of the wave. Overall, BDF2 performs best for this test case since it has the best balance between acoustic damping properties and accuracy.

7. Conclusions

In this paper we have analysed several time integration methods for the compressible two-fluid model with the goal to simulate stratified wavy flow and slug flow in pipelines in a so-called ‘slug capturing’ approach. The study was focussed on obtaining insight into the numerical pitfalls and requirements. Thereto a theoretical analysis on the differential equations and the discretized equations was given, in particular with respect to their stability properties. The analysis has been demonstrated for a number of test cases.

We conclude that the BDF2 method is a robust time integrator for the two-fluid model and it outperforms the commonly used Backward Euler method and the second order Crank–Nicolson method. This is due to a combination of its second order accuracy, A -stability and L -stability. These properties make that BDF2 can be used for the time integration of unsteady problems with a CFL number of 1 based on the liquid velocity, while not suffering from numerical oscillations that arise from acoustic wave propagation.

To facilitate the comparison and understanding of the time integration methods, several techniques have been proposed which have not been applied to the two-fluid model before. First, the eigenvalues of the spatial discretization have been investigated and it is shown how the stiffness depends linearly on the speed of

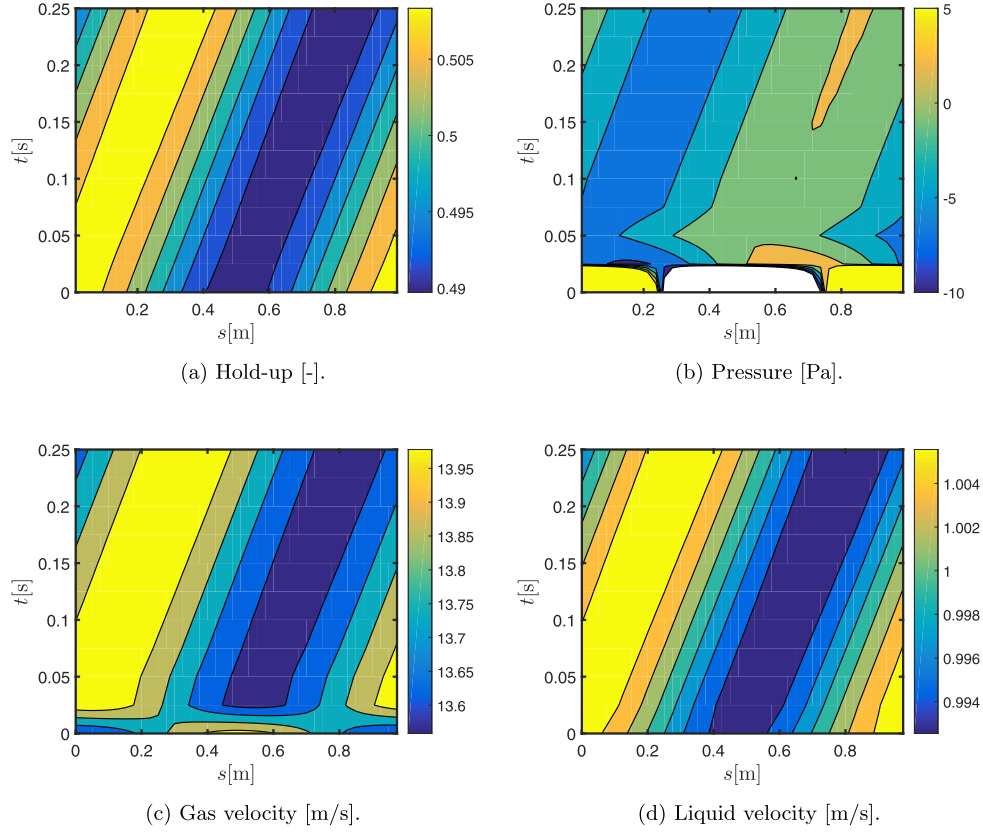


Fig. 17. Solution of acoustic wave problem in $s-t$ diagrams. BDF2, $C_l=1$.

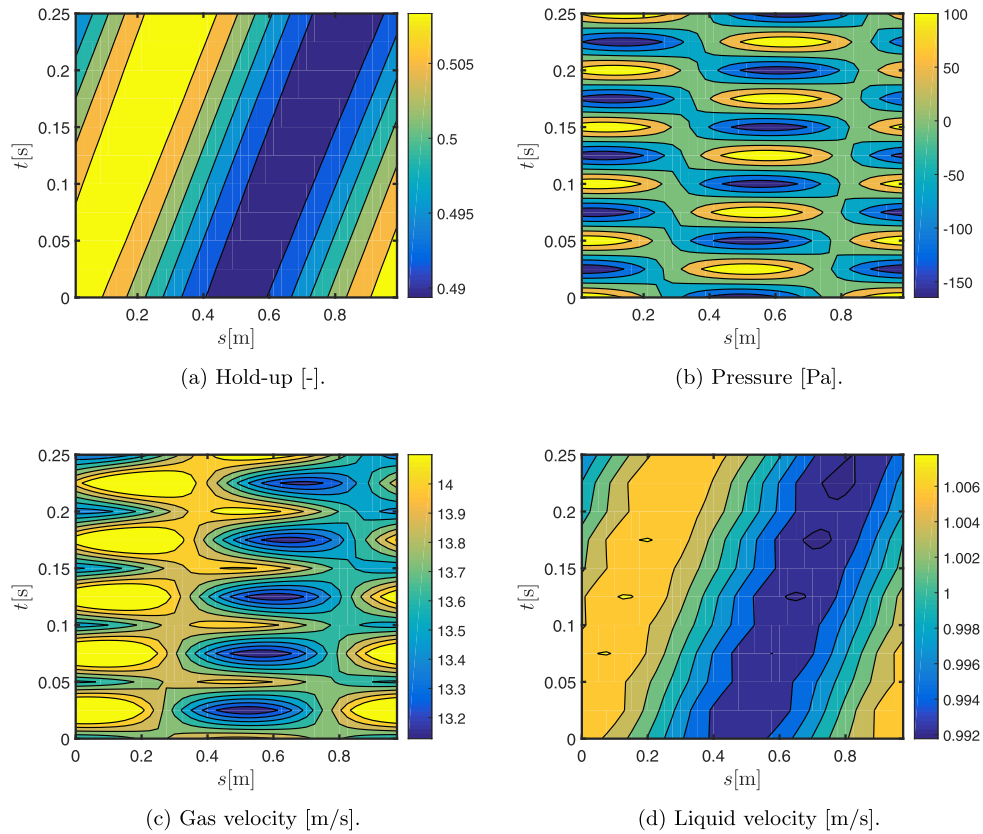


Fig. 18. Solution of acoustic wave problem in $s-t$ diagrams. Crank-Nicolson, $C_l=1$.

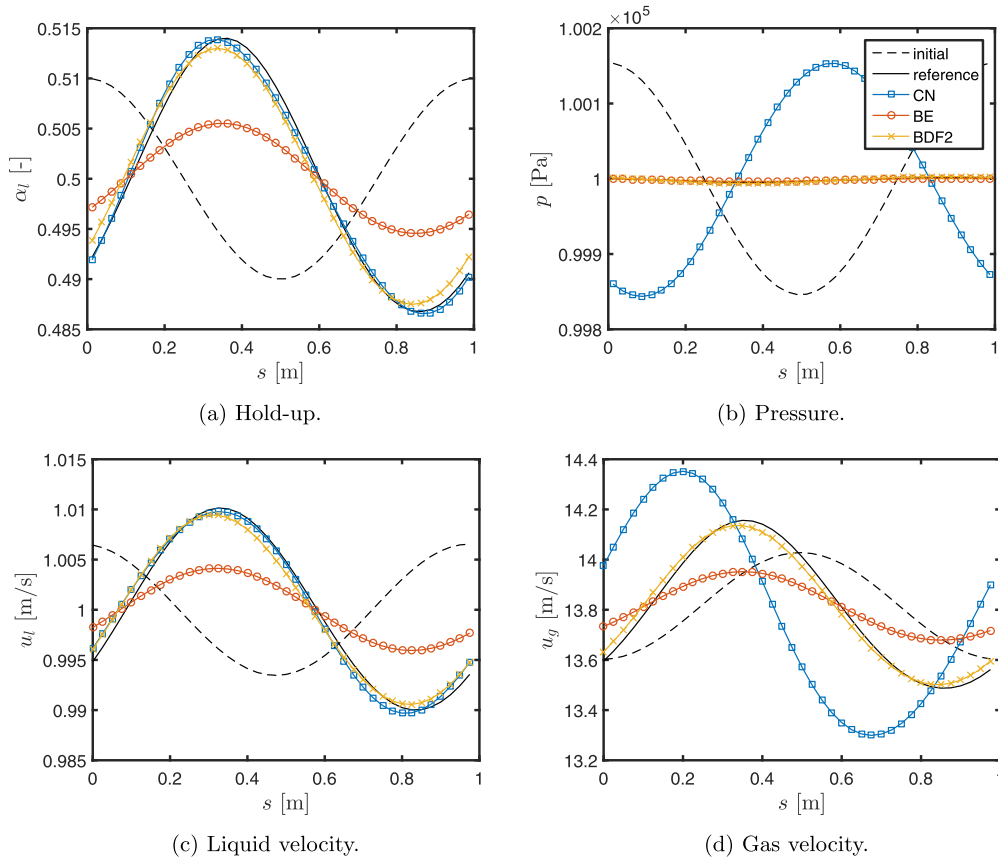


Fig. 19. Comparison of time integration methods at $t = 1$ s for double wave problem with $C_l = 1$.

sound and on the number of grid points. The central scheme is more accurate than the upwind scheme and captures the unstable region accurately. The comparison of the stability regions of the time integration methods shows the difference in damping properties between Backward Euler or BDF2 and Crank–Nicolson. Second, a new automatic von Neumann analysis technique has been developed as tool for direct evaluation of the stability of the discrete models by running a computer code without requiring symbolic manipulations. This makes it very flexible since it can be directly applied when more physics (e.g. surface tension or axial diffusion) or other spatial discretization methods are included. Third, we have proposed the use of Discrete Flow Pattern Maps (DFPM) to indicate to what extent discretization methods (for a certain choice of the number of grid points and the size of the time step) are able to reproduce the flow pattern maps that are based on the stability of the differential equations.

Several test cases have been used in which these techniques are used to compare BDF2 to other time integration methods: linear, nonlinear and acoustic Kelvin–Helmholtz instabilities. Accuracy tests and von Neumann analysis have shown its second order accuracy and comparable stability properties as Crank–Nicolson. BDF2 is slightly more diffusive than Crank–Nicolson but much more accurate than Backward Euler. The acoustic wave test shows that BDF2 is able to give accurate solutions, whether acoustic waves are resolved or not, whereas Crank–Nicolson leads to non-physical solutions. The ability of BDF2 to handle unresolved transients will also be important when dealing with other types of stiffness, for example caused by terms with small time scales (e.g. phase transition) or algebraic equations (e.g. the drift-flux model).

The Discrete Flow Pattern Map reveals that the *effective* well-posed unstable region is well captured by BDF2 but completely missed by Backward Euler, at least for the considered grid and time step resolutions. Simulations in the nonlinear regime furthermore have indicated that ill-posedness can occur when starting from the unstable regime. The implication is that the actual well-posed unstable regime for nonlinear simulations can be much smaller than the theoretical one, which can limit the application of the two-fluid model for simulating the stratified-slug flow transition.

We note that the DFPM as presented here is based on simulations in an idealized setting, with a simple geometry, initial conditions, and boundary conditions. In future work we plan to employ the BDF2 method to further study the formation of slug flow and ill-posedness issues under actual pipeline conditions.

In this paper we have relied on relatively standard spatial discretization techniques, since the focus is on the time discretization methods. Improvements in the spatial discretization (for example a method based on a Roe linearization) are needed to resolve discontinuities accurately and to capture the transition to locally single phase (slug) flow. Since the analysis in this paper does not require special properties of the spatial scheme, we expect that BDF2 can be applied to such discretization schemes without difficulty.

Acknowledgements

The authors would like to thank Ruud Henkes for the fruitful discussions and suggestions. Furthermore, the work by the second and third author was made possible by a grant from Shell Projects & Technology, which is greatly appreciated.

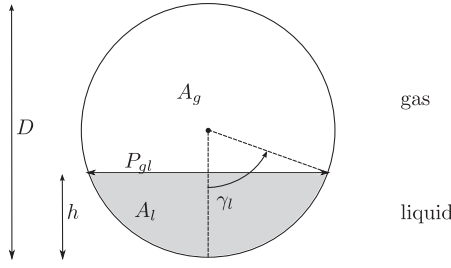


Fig. A.20. Stratified flow layout and definitions.

Appendix A. Two-fluid model details

A.1. Geometry

The following geometric identities are used to express the wall perimeters, interfacial perimeter, and liquid height in terms of the wetted angle γ_l (Fig. A.20):

$$P_{gl} = D \sin \gamma_l, \quad (\text{A.1})$$

$$P_l = D \gamma_l, \quad (\text{A.2})$$

$$P_g = D(\pi - \gamma_l), \quad (\text{A.3})$$

$$h = \frac{1}{2}D(1 - \cos \gamma_l). \quad (\text{A.4})$$

We use Biberg's approximation (Biberg, 1999) to express α_l in terms of γ_l (this avoids the iterative solution of a nonlinear equation):

$$\gamma_l = \pi \alpha_l + \left(\frac{3\pi}{2} \right)^{\frac{1}{3}} \left(1 - 2\alpha_l + \alpha_l^{\frac{1}{3}} - \alpha_g^{\frac{1}{3}} \right). \quad (\text{A.5})$$

A.2. Friction models

The wall (subscript w) and interfacial (subscript gl) shear stress are expressed by the Fanning friction factor definition:

$$\tau = \begin{cases} \frac{1}{2} f_\beta \rho_\beta u_\beta |u_\beta| & \text{wall} \\ \frac{1}{2} f_{gl} \rho_g (u_\beta - u_\gamma) |u_\beta - u_\gamma| & \text{interfacial} \end{cases} \quad (\text{A.6})$$

The friction factor f_β of phase β with the pipe wall is modeled with the Churchill relation (Churchill, 1977):

$$f_\beta = 2 \left(\left(\frac{8}{\text{Re}_\beta} \right)^{12} + (A + B)^{-1.5} \right)^{\frac{1}{12}}, \quad (\text{A.7})$$

$$A = \left(2.457 \ln \left(\left(\left(\frac{7}{\text{Re}_\beta} \right)^{0.9} + 0.27 \frac{\epsilon}{D_{h\beta}} \right)^{-1} \right) \right)^{16}, \quad (\text{A.8})$$

$$B = \left(\frac{37530}{\text{Re}_\beta} \right)^{16}. \quad (\text{A.9})$$

Here ϵ is the hydraulic pipe roughness, Re_β is the Reynolds number,

$$\text{Re}_\beta = \frac{\rho_\beta u_\beta D_{h\beta}}{\mu_\beta}, \quad (\text{A.10})$$

and $D_{h\beta}$ is the hydraulic diameter:

$$D_{h\beta} = \begin{cases} \frac{4A_l}{P_{hw}} & \text{if } \beta = l \\ \frac{4A_g}{P_{gw} + P_{gl}} & \text{if } \beta = g \end{cases} \quad (\text{A.11})$$

The interfacial friction factor f_{gl} is calculated by (Liao et al., 2008):

$$f_{gl} = \max\{f_g, 0.014\}. \quad (\text{A.12})$$

References

- Akselsen, A.H., 2016. A linear stability analyses of discrete representations of the two-fluid model for stratified two-phase flow. In: *Proceedings of the 9th International Conference on Multiphase Flow*, May 22nd–27th ICMF-2016, Firenze, Italy.
- Akselsen, A.H., 2016. Efficient Numerical Methods for Waves in One-Dimensional Two-Phase Pipe Flows. (Ph.D. thesis). NTNU.
- Barnea, D., Taitel, Y., 1993. Kelvin–Helmholtz stability criteria for stratified flow: viscous versus non-viscous (inviscid) approaches. *Int. J. Multiph. Flow* 19 (4), 639–649. doi:10.1016/0301-9322(93)90092-9.
- Barnea, D., Taitel, Y., 1994. Interfacial and structural stability of separated flow. *Int. J. Multiph. Flow* 20 (94), 387–414.
- Bendiksen, K., Malnes, D., Moe, R., Nuland, S., 1991. The dynamic two-fluid model OLGA: theory and application. *SPE Prod. Eng.* 1991 6 (SPE-19451), 171–180.
- Berry, R. A., Zou, L., Zhao, H., Zhang, H., Peterson, J. W., Martineau, R. C., Kadioglu, S. Y., Andrs, D., 2015. RELAP-7 Theory manual - INL/EXT-14-31366.
- Biberg, D., 1999. An explicit approximation for the wetted angle in two-phase stratified pipe flow. *Can. J. Chem. Eng.* 77 (3), 1221–1224.
- Bonizzi, M., 2003. Transient One-Dimensional Modelling of Multiphase Slug Flows. (Ph.D. thesis). Imperial College.
- Butcher, J.C., 2003. Numerical Methods for Ordinary Differential Equations. John Wiley & Sons, Ltd. doi:10.1002/0470868279.
- Churchill, S.W., 1977. Friction-factor equation spans all fluid flow regimes. *Chem. Eng.* 84 (24), 91–92.
- Danielson, T.J., Bansal, K.M., Hansen, R., Leporcher, E., 2005. LEDA: the next multiphase flow performance simulator. In: *BHR Group 2005 Multiphase Production Technology* 12, pp. 477–492.
- Drew, D.A., Passman, S.L., 1998. *Theory of Multicomponents Fluids*. Springer.
- Evje, S., Flåtten, T., 2003. Hybrid flux-splitting schemes for a common two-fluid model. *J. Comput. Phys.* 192 (1), 175–210. doi:10.1016/j.jcp.2003.07.001.
- Figueiredo, A.B., Baptista, R.M., de Freitas Rachid, F.B., Bodstein, G.C.R., 2017. Numerical simulation of stratified-pattern two-phase flow in gas pipelines using a two-fluid model. *Int. J. Multiph. Flow* 88, 30–49. doi:10.1016/j.ijmultiphaseflow.2016.09.016.
- Fitt, A.D., 1989. The numerical and analytical solution of ill-posed systems of conservation laws. *Appl. Math. Model.* 13, 618–631.
- Fullmer, W.D., Ransom, V.H., Lopez de Bertodano, M.A., 2014. Linear and nonlinear analysis of an unstable, but well-posed, one-dimensional two-fluid model for two-phase flow based on the inviscid kelvin–Helmholtz instability. *Nucl. Eng. Des.* 268, 173–184.
- Gottlieb, S., Shu, C.-W., Tadmor, E., 2001. Strong stability-preserving high-order time discretization methods. *SIAM Rev.* 43 (1), 89–112. doi:10.1137/S003614450036757X.
- Hairer, E., Norsett, S.P., Wanner, G., 2008. *Solving Ordinary Differential Equations I*. Springer. doi: 10.1007/978-3-540-78862-1.
- Hendrix, M.H.W., Smith, I.E., van Zwieten, J.S.B., Sanderse, B., 2016. Comparison of numerical methods for slug capturing with the two-fluid model. In: *ICMF-2016 - 9th International Conference on Multiphase Flow May 22nd - 27th 2016, Firenze, Italy*.
- Hirsch, C., 1994. *Numerical Computation of Internal and External Flows - Volume 1, Fundamentals of Numerical Discretization*. Wiley.
- Holmås, H., 2008. Numerical Simulation of Waves in Two-Phase Pipe Flow Using 1D Two-Fluid Models. (Ph.D. thesis). University of Oslo.
- Holmås, H., 2010. Numerical simulation of transient roll-waves in two-phase pipe flow. *Chem. Eng. Sci.* 65 (5), 1811–1825. doi:10.1016/j.ces.2009.11.031.
- Hundsdofer, W., Verwer, J., 2007. *Numerical Solution of Time-Dependent Advection–Diffusion–Reaction Equations*, 33. Springer. doi: 10.1007/978-3-662-09017-6.
- Issa, R.I., Kempf, M.H.W., 2003. Simulation of slug flow in horizontal and nearly horizontal pipes with the two-fluid model. *Int. J. Multiph. Flow* 29 (1), 69–95. doi:10.1016/S0301-9322(02)00127-1.
- Johnson, G. W., 2005. A Study of Stratified Gas–Liquid Pipe Flow. (Ph.D. thesis). University of Oslo.
- Kjølaas, J., De Leebeeck, A., Johansen, S.T., 2013. Simulation of hydrodynamic slug flow using the Ledaflow slug capturing model. In: *Proceedings of the 16th International Conference on Multiphase Production Technology*, 12–14 June, Cannes, France.
- Liao, J., Mei, R., Klausner, J.F., 2008. A study on the numerical stability of the two-fluid model near ill-posedness. *Int. J. Multiph. Flow* 34 (11), 1067–1087. doi:10.1016/j.ijmultiphaseflow.2008.02.010.
- López de Bertodano, M., Fullmer, W., Clausse, A., Ransom, V.H., 2017. *Two-Fluid Model Stability, Simulation and Chaos*. Springer doi:10.1007/978-3-319-44968-5.

- Lopez-de-Bertodano, M., Fullmer, W., Vaidheeswaran, A., 2013. One-dimensional two-equation two-fluid model stability. *Multiph. Sci. Technol.* 25 (2–4), 133–167. doi:10.1615/MultScienTechn.v25.i2-4.60.
- Lyczkowski, R.W., Gidaspow, D., Solbrig, C.W., Hughes, E.D., 1978. Characteristics and stability analyses of transient one-dimensional two-phase flow equations and their finite difference approximations. *Nucl. Sci. Eng.* 66 (3), 378–396. doi:10.13182/nse78-4.
- Masella, J.M., Tran, Q.H., Ferre, D., Pauchon, C., 1998. Transient simulation of two-phase flows in pipes. *Int. J. Multiph. Flow* 24 (5), 739–755. doi:10.1016/S0301-9322(98)00004-4.
- Montini, M., 2011. Closure Relations of the One-Dimensional Two-Fluid Model for the Simulation of Slug Flows. (Ph.D. thesis). Imperial College.
- Morin, A., Flåtten, T., Munkejord, S.T., 2013. A Roe scheme for a compressible six-equation two-fluid model. *Int. J. Numer. Methods Fluids* 72, 478–504. doi:10.1002/fld.
- Morton, K.W., Mayers, D., 2005. *Numerical Solution of Partial Differential Equations*. Cambridge University Press.
- Prosperetti, A., Tryggvason, G., 2007. *Computational Methods for Multiphase Flow*. Cambridge University Press.
- Ramshaw, J.D., Trapp, J.A., 1978. Characteristics, stability, and short-wavelength phenomena in two-phase flow equation systems. *Nucl. Sci. Eng.* 66, 93–102.
- Ransom, V.H., Hicks, D.L., 1984. Hyperbolic two-pressure models for two-phase flow. *J. Comput. Phys.* 53, 124–151.
- Ransom, V.H., Hicks, D.L., 1988. Hyperbolic two-pressure models for two-phase flow revisited. *J. Comput. Phys.* 75, 498–504.
- Song, J., 2003. A remedy for the ill-posedness of the one-dimensional two-fluid model. *Nucl. Eng. Des.* 222 (1), 40–53. doi:10.1016/S0029-5493(02)00391-6.
- Song, J.H., Ishii, M., 2001. One-dimensional two-fluid model with momentum flux parameters. *Nucl. Eng. Des.* 205, 145–158. doi:10.1016/S0029-5493(00)00351-4.
- Stewart, H.B., Wendroff, B., 1984. Two-phase flow: models and methods. *J. Comput. Phys.* 56, 363–409.
- Toumi, I., Kumbharo, A., 1996. An approximate linearized Riemann solver for a two-fluid model. *J. Comput. Phys.* 124, 286–300.
- Wallis, G.B., 1969. *One-Dimensional Two-Phase flow*. McGraw-Hill.
- Whitham, G.B., 1974. *Linear and Nonlinear Waves*. Wiley, New York.
- Zou, L., Zhao, H., Zhang, H., 2015. Applications of high-resolution spatial discretization scheme and Jacobian-free Newton–Krylov method in two-phase flow problems. *Ann. Nucl. Energy* 83, 101–107. doi:10.1016/j.anucene.2015.04.016.
- van Zwieten, J.S.B., Sanderse, B., Hendrix, M.H.W., Vuik, C., Henkes, R.A.W.M., 2015. Efficient simulation of one-dimensional two-phase flow with a new high-order Discontinuous Galerkin method, Report 15-07. Technical Report. Delft University of Technology.